Journal of Geophysical Research: Atmospheres

RESEARCH ARTICLE
10.1029/2017JD027808

The Climatological Effect of Saharan Dust on Global Tropical Cyclones in a Fully Coupled GCM

Jeffrey D. O. Strong[1], **Gabriel A. Vecchi**[2,3], **and Paul Ginoux**[4]

[1]Lamont-Doherty Earth Observatory of Columbia University, Palisades, NY, USA, [2]Department of Geosciences, Princeton University, Princeton, NJ, USA, [3]Princeton Environmental Institute, Princeton University, Princeton, NJ, USA, [4]NOAA/Geophysical Fluid Dynamics Laboratory, Princeton, NJ, USA

Key Points:
- Modeled Saharan dust decreases tropical cyclone frequency across the North Atlantic
- The simulated effect strongly depends on the amount of aerosol absorption versus scattering
- Saharan dust can impact tropical cyclones beyond the Atlantic through atmospheric teleconnection patterns

Supporting Information:
- Supporting Information S1

Correspondence to:
J. D. O. Strong,
js5261@columbia.edu

Citation:
Strong, J. D. O., Vecchi, G. A., & Ginoux, P. (2018). The climatological effect of Saharan dust on global tropical cyclones in a fully coupled GCM. *Journal of Geophysical Research: Atmospheres*, *123*, 5538–5559. https://doi.org/10.1029/2017JD027808

Received 4 OCT 2017
Accepted 15 APR 2018
Accepted article online 8 MAY 2018
Published online 31 MAY 2018

Abstract Climate in the tropical North Atlantic and West Africa is known to be sensitive to both the atmospheric burden and optical properties of aerosolized mineral dust. We investigate the global climatic response to an idealized perturbation in atmospheric burden of Saharan-born mineral dust, comparable to the observed changes between the 1960s and 1980s, using simulations with the high-resolution, fully coupled Geophysical Fluid Dynamics Laboratory Climate Model 2.5, Forecast-oriented Low Ocean Resolution version, across a range of realistic optical properties, with a specific focus on tropical cyclones. The direct radiative responses at the top of the atmosphere and at the surface along with regional hydrologic and thermodynamic responses are in agreement with previous studies, depending largely on the amount of aerosol absorption versus scattering. In all simulations, dust causes a decrease in tropical cyclone activity across the North Atlantic Ocean, as determined by a tropical cyclone tracking scheme, with the largest response occurring in the most absorbing and scattering optical regimes. These changes are partially corroborated by common local genesis potential indices. However, no clear-cut explanation can be developed upon inspection of their constituent variables. There are also nonnegligible anomalies in the North Pacific and Indian Oceans in these simulations. A relationship between accumulated cyclone energy and top of the atmosphere radiative flux anomalies is used to explain the North Atlantic anomalies, while analogy to known climate variations can help us understand the far-field response to the dust forcing.

1. Introduction

Mineral dust primarily originates from arid or semiarid regions of the world (Prospero et al., 2002) where surface winds lift soil particles into the atmosphere (Gillette et al., 1980). Once suspended, these particles can be advected thousands of kilometers away from their point of origin (Grousset et al., 2003). North Africa, and in particular the Sahara desert, is the largest contributor to global, aeolian dust in the world (Ginoux, Prospero, et al., 2012). Dust emissions from North Africa have a distinct seasonal cycle with the greatest areal extent occurring in Boreal summer and autumn (Adams et al., 2012). There is also evidence for significant interannual (Ridley et al., 2014) and multidecadal scale variability (Mahowald et al., 2010) in dust transport from North Africa. For example, surface dust concentrations as measured at Barbados increased almost five times between the 1960s and 1980s (Prospero & Lamb, 2003). In addition, Saharan-born dust is commonly not of a single homogeneous composition but is instead a combination of multiple regional mineral deposits (Caquineau et al., 2006).

The choice of mineralogy data set has been shown to considerably affect the calculated interaction of dust with radiation (Sokolik & Toon, 1999). In general, dust increases the shortwave attenuation of the atmosphere due to both scattering and absorption, which leads to a decrease in net shortwave radiative flux at the surface (Tegen & Lacis, 1996). Simultaneously, mineral dust also affects the longwave radiative flux through the atmosphere (Volz, 1973). These effects combine and lead to a redistribution of radiative heating of the atmospheric column (Miller et al., 2014). This direct radiative effect has been modeled and shown to influence the climate in numerous studies (Colarco et al., 2014; Miller & Tegen, 1998; Miller et al., 2014; Strong et al., 2015; Yoshioka et al., 2007). In addition, mineral dust has been shown to affect cloud microphysics (DeMott et al., 2003; Levin et al., 1996) and biogeochemistry of both the land (Swap et al., 1992)

and ocean (Jickells et al., 2005). These climatologically important changes can further modulate the impact of dust on such human-important phenomena as air pollution (Liu et al., 2009) and tropical cyclone frequency (Dunion & Velden, 2004).

There is growing evidence of the impact of mineral dust on individual tropical cyclone genesis and development both observationally (Braun, 2010; Evan et al., 2006; Sun et al., 2008) and with models (Bretl et al., 2015; Karyampudi & Pierce, 2002; Reale et al., 2014; Zhang et al., 2007, 2009). Due to the large-scale influence of mineral dust, it can potentially have both positive and negative impacts on the development of tropical cyclones. For instance, the development of thermally driven easterly jets can act to increase the genesis frequency of tropical cyclones along the jet's southern border (Braun, 2010). Conversely, the significant drying and heating aloft, surface cooling, and increased wind shear can dampen the probability of tropical cyclone genesis (Dunion & Velden, 2004). There is also a growing body of evidence attempting to link atmospheric dust load and tropical cyclone frequency on climatological timescales (Wang et al., 2012). However, there has been little work in modeling these relationships in a fully coupled framework on climatologically relevant timescales.

The purpose of this study then is to investigate the coupled atmospheric and oceanic climatological effect of Saharan dust's radiative forcing on tropical cyclones. To this end, we will use a state of the art general circulation model run at a high enough resolution to adequately resolve tropical cyclones. Based on the results shown in previous literature that increased attenuation of solar radiation by dust aerosols leads to strong local surface cooling and the significant correlation between hurricane activity and sea surface temperature anomalies, our hypothesis is that Saharan-born dust will cause a significant decrease in tropical cyclone frequency across the North Atlantic Ocean for the full range of investigated optical regimes and with diminishing significant results farther from the main dust plume.

The paper is organized as follows. In section 2 we describe the model, computations, and data sets used in this study as well as the experimental design. In section 3 we discuss the global radiation, surface temperature, and precipitation response to perturbations in Saharan-born dust, principally for comparison with other studies. In section 4 we analyze the global changes to tropical cyclone density and compare them with the observational record as well as several common genesis forecast indices. In section 5 we explore changes to several regional factors, which could influence the modeled anomalies in tropical cyclogenesis and development and craft several hypotheses for the modeled changes. In section 6 we present a discussion of the results and our concluding remarks.

2. Methodology

Our study follows, in most parts, the same experimental protocol set forth by Strong et al. (2015). It features improvements to both the modeling framework and sensitivity range of optical properties used for modeling dust's radiative forcing as well as streamlining the calculation of dust's impact on the climate.

2.1. Coupled Model

For this study, we used the Geophysical Fluid Dynamics Laboratory's (GFDL) Coupled Model CM2.5 Forecast-oriented Low Ocean Resolution version (CM2.5-FLOR; Vecchi et al., 2014) to calculate the effect of perturbations to the atmospheric aerosol burden of dust under various optical regimes. GFDL's CM2.5-FLOR is an offshoot of the previous Coupled Model v2.5 (CM2.5; Delworth et al., 2012) developed at GFDL and uses many of the same model configurations. The atmosphere and land components have a horizontal resolution of 0.5° by 0.5° using a cubed-sphere, finite-volume dynamical core. This resolution has been shown to adequately resolve the distribution of tropical-cyclone-like vortices (TCs; Vecchi et al., 2014) but is deficient in its ability to resolve the most intense TCs (Murakami et al., 2015). Atmospheric aerosol and gas concentrations as well as land cover are specified. Only the direct radiative effect of aerosols is calculated in the model. The ocean and ice components use a lower 1° horizontal resolution that enhances to 1/3° near the equator. This model framework shows substantial improvement to its climate simulations relative to the previous Coupled Model v2.1 and marginal improvements relative to CM2.5 (Jia et al., 2015). However, CM2.5-FLOR still suffers from some common TC-resolving general circulation model (GCM) issues (Vecchi et al., 2014). For example, there are too many cyclones in the central North Pacific, Southern Hemisphere, and Indian Ocean and too few cyclones In the North Atlantic particularly in the Caribbean and Gulf of Mexico.

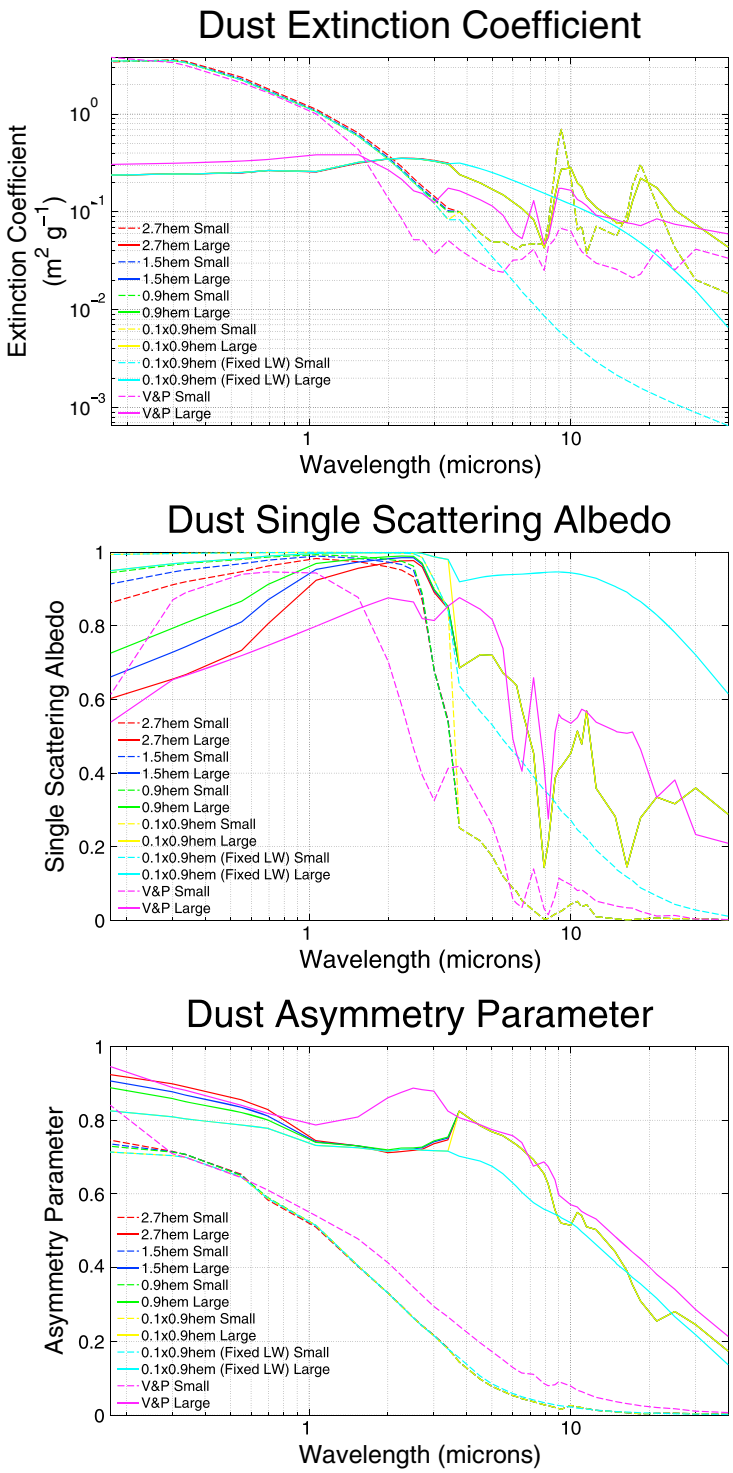

Figure 1. The optical properties of all regimes of dust used in this experiment. The values are averaged over the fine (small) dust bin sizes (0.1, 0.2, 0.4, and 0.8 μm; dashed lines) and the coarse (large) dust bin sizes (1, 2, 4, and 8 μm; solid lines). The top panel (a) shows the extinction coefficient (m^2/g) as a function of wavelength. The middle panel (b) shows the single scattering albedo of the dust as a function of wavelength. The bottom panel (c) shows the asymmetry parameter of the dust as a function of wavelength.

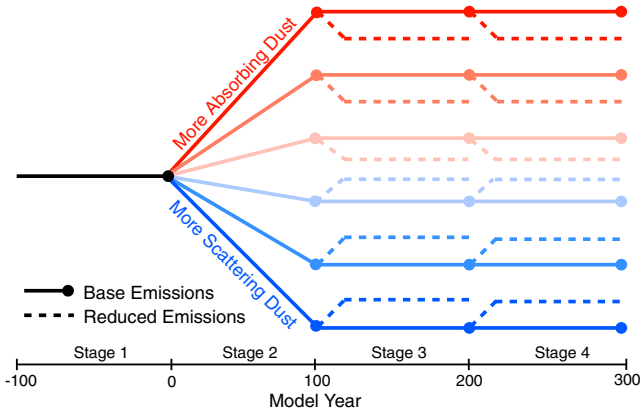

Figure 2. A schematic diagram of the layout of model simulations conducted for this experiment. Stage 1 consists of the model "spin-up" period. Stage 2 is when six different control simulations, based on the dust optical properties, are run to equilibrium. Stages 3 and 4 include the principal model simulations where the model is run with both base and reduced dust emissions in parallel.

2.2. Dust Forcing

We use the same prescribed climatological annual cycles of monthly, global mineral dust aerosol burden as in Figure 2 of Strong et al. (2015; Figure S1 in the supporting information). Both climatological cycles were calculated using the Model of Ozone and Related Chemical Tracers, version 2 (Horowitz, 2006; Horowitz et al., 2003; Tie et al., 2005) forced by the National Centers for Environmental Prediction-National Center for Atmospheric Research reanalysis of 1990 (Jickells et al., 1996). The base cycle used the full emission values over North Africa whereas the reduced cycle lowered emission values over the entirety of North Africa to 20% of their calculated values. These climatologies are meant to represent the high and low dust concentrations of the 1980s and 1960s, respectively.

We increased the range of optical properties used to calculate the modeled radiative forcing of dust from the two values of Strong et al. (2015) to now incorporate six optical regimes, the properties of which are detailed in Figure 1. The first regime (V&P) is derived from a combination of the in situ observations of Volz (1973) and Patterson et al. (1977). This combination has been used in previous GFDL climate models (Anderson et al., 2004) and is the same as the absorbing-dust case of Strong et al. (2015). However, this optical regime has been found to be overly absorbing (Sinyuk et al., 2003), and so the remaining optical regimes are calculated using Mie theory with the refractive indices given by Balkanski et al. (2007). We consider the cases of 2.7% (2.7hem), 1.5% (1.5hem), and 0.9% hematite concentration by volume (0.9hem), the first of which has been used in a previous GFDL climate model (Donner et al., 2011). In addition, we create two other artificial optical regimes aimed at replicating extremely scattering mineral dust. For the first regime, we multiply the imaginary part of the refractive index of the 0.9hem case by 0.1 (0.1×0.9hem), and for the second regime, we set the longwave refractive index of the 0.1×0.9hem case to a constant value (0.1×0.9hem fixed longwave [LW]). This latter optical regime is the same as the scattering-dust case of Strong et al. (2015).

2.3. Experimental Design

The model is initialized in a spun-up state following 100 years of forcing with an invariant 1990 climatology of insolation, gas and aerosol concentrations, and land cover as described by Vecchi et al. (2014) (Stage 1, Figure 2). We create a control state for each of the six optical regimes using the base dust climatology and run each individually for 100 years to allow the climate system to further equilibrate (Stage 2, Figure 2). We then run each control simulation for a further 200 years. Using the climate state at years 100 and 200 as initialization we create two perturbation simulations for each optical regime where we keep the optical properties the same but change the dust climatology for the annual cycle of atmospheric dust load to the reduced emission state. Each of these perturbations is allowed to run for 100 years in parallel to their respective control simulations (Stages 3 and 4, Figure 2). To calculate the impact of dust, we align the control and perturbation simulations by equivalent model year and then subtract the perturbation simulations from their respective control simulations to arrive at a value representative of the impact of adding a realistic amount of Saharan dust aerosol burden to the atmosphere.

2.4. Tropical Cyclone Tracker

Using the model's 6-hourly output, we track simulated TCs with the method described by Zhao et al. (2009) and the parameter settings of Kim et al. (2014). The tracker has three steps that we briefly describe here. The first is to tag potential TCs by colocating local maxima in lower tropospheric relative vorticity and upper tropospheric temperature and local minima in sea level pressure. These colocated anomalies are then tracked in the output data. If they persist long enough, they are finally categorized by their wind speed as a tropical cyclone. In calculating the density of TCs, we first create a 1° by 1° global grid and then define the TC track density as the number of days with a TC present in a box 10° by 10° centered on each 1° grid cell. This is for several reasons as described by Vecchi et al. (2014): The size of the $10° \times 10°$ grid is much smaller than the scale of the basins, on a scale comparable to the average diameter of observed TCs (Chavas & Emanuel, 2010) and is large enough to include most of the areas where impacts of individual TCs in models are evident (Lin et al., 2010). The choice of grid size also minimizes the impact of the edges of larger discrete boxes

in computing density, effectively smoothing the field of TC density. Similarly, we define the TC genesis density as the number of TCs whose first registration by the TC tracking scheme occurs in the same 10° by 10° box centered on each 1° grid cell.

To focus on the mean response, we implement a bootstrap, without replacement, style calculation to determine the dust-induced changes in TC density and genesis. For each grid cell, we construct a time series of the annual sum of TC density or genesis in both the base and reduced dust cycle experiments. The order of these time series is randomized, and then the reduced dust series is subtracted from the base dust series, and the result is averaged. This process is repeated 1,000,000 times on the original time series, and the resultant set of 1,000,000 values is averaged to produce a single value for that grid cell. The results are not fundamentally different from doing a strict anomaly calculation between the base and reduced dust climatologies but do highlight the most significant responses.

3. Mean Climate State Anomalies

For comparison with other studies, we begin by analyzing the Saharan dust induced changes to the global climate as detailed in several common radiative and thermodynamic variables. The responses in the areas directly under the dust plume were more thoroughly analyzed in a previous paper (Strong et al., 2015) and will be noted here for model intercomparison purposes. The following results are all averaged over the Boreal summer and autumn seasons (June–November) as this time frame contains the entirety of and is roughly centered on the active seasons for both the areal extent of the Saharan dust plume (Adams et al., 2012) as well as the Northern Hemisphere tropical cyclone season. The general results do not change significantly when considering the annual average.

3.1. Top of the Atmosphere Net Radiative Flux Anomalies

We observe in our model simulations that Saharan-born dust causes significant anomalies in the net clear-sky radiative flux at the top of the atmosphere (ToA; Figures 3a–3f and Table S1, first column). The largest anomalies, and simultaneous largest discrepancies between optical regimes, occur over much of North and West Africa in regions most directly influenced by the changes in atmospheric dust burden.

In the most absorbing cases (Figures 3a–3d) we note a strong positive anomaly along the western Sahara/Sahel boundary, peaking to the north of Lake Chad at over 20 W/m^2 in the V&P regime (Figure 3a). This is largely due to the shortwave component of the net radiative flux. The increased absorption relative to scattering of shortwave radiation by dust decreases the net column albedo over the relatively high albedo Sahara desert. This allows less shortwave radiation to be reflected back to space and leads to the positive ToA anomaly.

This positive anomaly begins to slowly transition as the optical regime becomes more scattering. As the scattering ability of dust increases, the dust aerosol plume brightens relative to the surface. Beginning in the 1.5hem (Figure 3c) and 0.9hem (Figure 3d) dust cases, we note a negative ToA radiative flux anomaly developing in the region between 5°N–15°N and 15°W–15°E, hereafter referred to as the West African monsoon (WAM) region. This occurs as the dust aerosol becomes more reflective than the surface.

As we continue to increase the scattering ability of the dust to the 0.1×0.9hem (Figure 3e) and 0.1×0.9hem (fixed LW; Figure 3f) cases, we develop a strong negative anomaly across much of North and West Africa, peaking around −20 W/m^2 along the southern Sahara desert. This negative anomaly is primarily due to the shortwave scattering of dust increasing the net column albedo over these regions, beginning with the relatively low-albedo WAM region in the 1.5hem and 0.9hem cases and extending to much higher albedo over the Sahara desert in the most scattering cases.

In all optical regimes, we observe a strong negative anomaly across much of the tropical North Atlantic Ocean, even stretching across the Caribbean Sea and portions of Central America. The largest anomalies are focused in the eastern tropical North Atlantic, just off the coast of West Africa, and fade both westward and poleward/equatorward the farther we look from the main atmospheric dust plume. This is again due to the increased brightness of dust relative to the low albedo ocean surface. This effect is emphasized as the anomalies increase in magnitude as the dust becomes more scattering.

There are also far-field ToA radiative flux anomalies, particularly across the Himalayas, Indian subcontinent, and in the polar regions. These anomalies are due to changes in surface temperature affecting the column

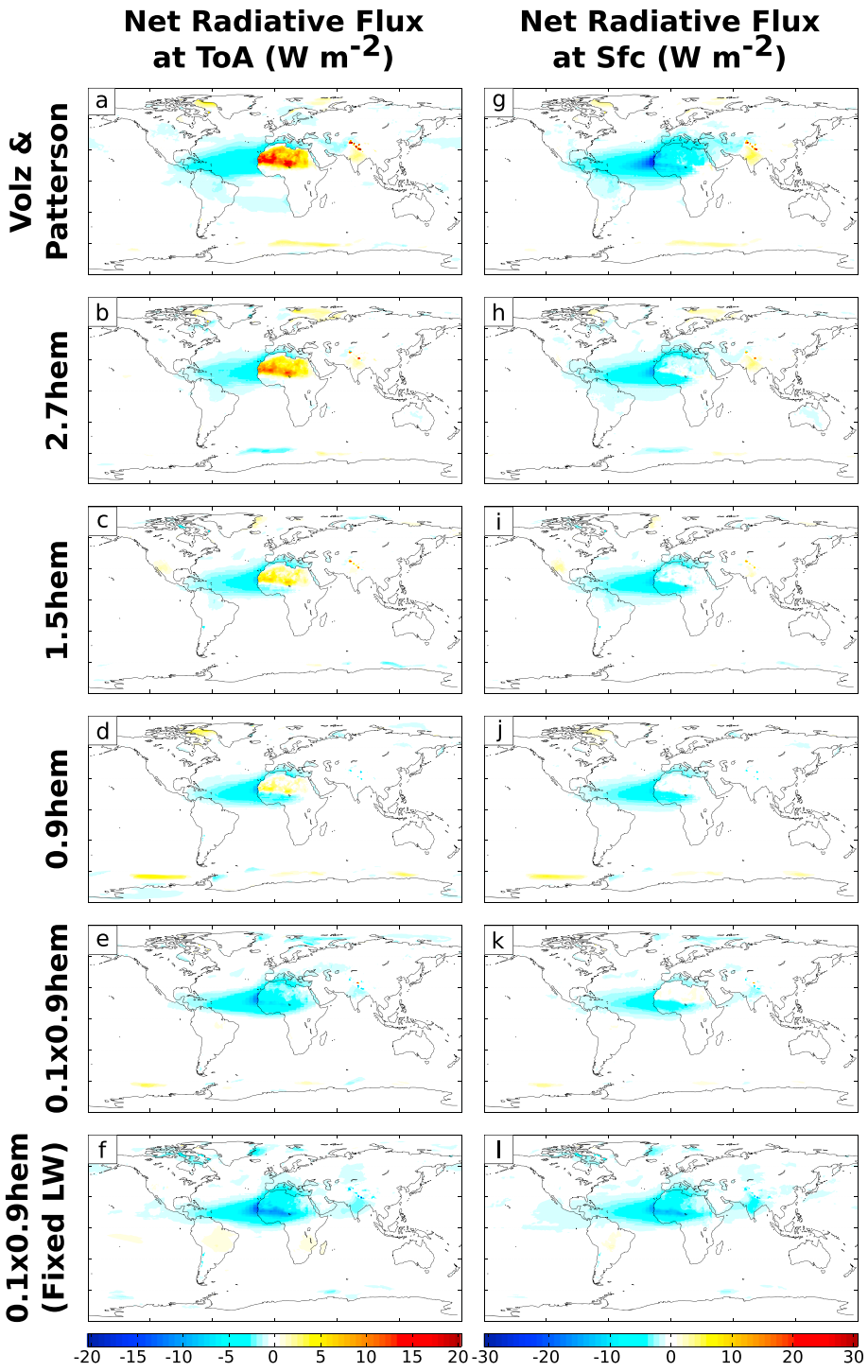

Figure 3. The global radiative anomalies due to an increase in Saharan dust, comparable to the observed changes between the 1960s and 1980s, with differing optical properties. The values are averaged over June–November and only those values that pass a Student's *t* test to 95% are shaded. The columns, from left to right, show the net radiative flux anomalies at the top of the atmosphere (positive downward; watts per square meter) and the net radiative flux anomalies at the surface (positive downward; watts per square meter). The rows, from top to bottom, show the response in the V&P, 2.7hem, 1.5hem, 0.9hem, 0.1 × 0.9hem, and 0.1 × 0.9hem (fixed longwave [LW]) optical regimes and are ordered by increased scattering of dust.

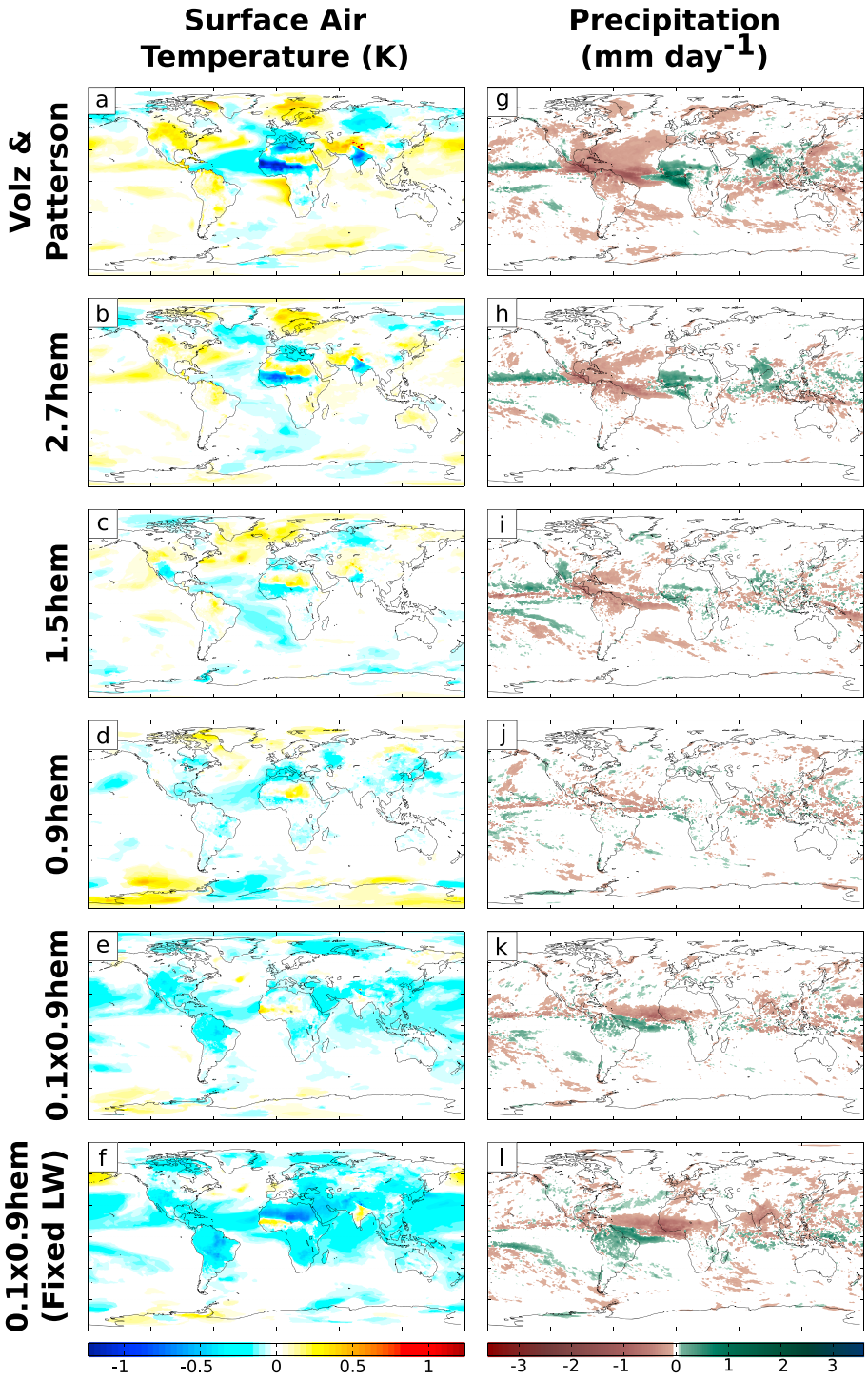

Figure 4. The global anomalies due to an increase in Saharan dust, comparable to the observed changes between the 1960s and 1980s, with differing optical properties. The values are averaged over June–November and only those values that pass a Student's *t* test to 95% are shaded. The columns, from left to right, show the 2-m air temperature anomalies (K) and the precipitation anomalies (mm/day). The rows, from top to bottom, show the response in the V&P, 2.7hem, 1.5hem, 0.9hem, 0.1 × 0.9hem, and 0.1 × 0.9hem (fixed longwave [LW]) optical regimes and are ordered by increased scattering of dust.

radiative budget. In the Himalayas, the surface warming/cooling (Figures 4a–4f) decreases/increases the snowpack and alters the surface albedo leading to an increased/decreased net radiative flux at the ToA. The similar ToA radiative flux anomalies over the lowlands of the Indian subcontinent arise from the opposite surface temperature response in this region. The surface warm/cool anomalies lead to an increase/decrease in outgoing longwave radiation, which in turn causes a negative/positive ToA radiative flux anomaly. A quick approximation with the Stefan-Boltzmann law applied to the simulated changes in surface temperature give a radiative anomaly of the same order of magnitude.

Meanwhile, the polar responses in several polar seas are described by changes in surface temperature (Figures 4a–4f) and sea ice concentration in those areas. A decrease/increase in surface temperature leads to increased/decreased sea ice concentration, which in turn causes an increased/decreased surface albedo and a respective decrease/increase in net radiative flux at the ToA. These regional anomalies are beyond the scope of the current paper but deserve a more detailed analysis in later work.

3.2. Surface Net Radiative Flux Anomalies

Transitioning now to the surface radiative balance (Figures 3g–3l and Table S1, second column), we note the similarity in major spatial patterns between the net radiative flux at the surface and that at the ToA. The largest and most homogeneous response is negative and occurs across much of North and West Africa and stretches out across the tropical North Atlantic Ocean into Central America. This negative response is strongest in the most absorbing (Figure 3g) and the most scattering (Figure 3l) optical regimes with anomalies just off the West African coastline reaching over −30 W/m^2. The cause of these negative anomalies is the increased atmospheric attenuation of radiation provided by the aeolian dust particles. In all of the optical regimes, dust will both absorb and scatter shortwave radiation leading to a decreased radiative flux at the surface. In our model simulations, this effect is maximized when either the absorption or scattering properties of dust are maximized, thus leading to the largest anomalies being in the V&P and 0.1 × 0.9hem (fixed LW) cases.

We observe the same far-field anomalies in radiative flux at the surface as we did in the radiative flux response at the ToA. This includes the increased radiative flux over the Himalayas and Indian subcontinent in the most absorbing regimes (Figures 3g–3i), the decreased radiative flux over the Himalayas and Indian subcontinent in the most scattering regimes (Figures 3j–3l), and the assortment of anomalies across various polar seas. These anomalies appear in the surface budget as well as the ToA budget because they rely on the surface radiative budget changing, as stated prior, and not any associated radiative effects in the atmosphere.

3.3. Surface Temperature Anomalies

The 2-m surface air temperature anomalies due to changes in Saharan-born dust (Figures 4a–4f and Table S1, third column) extend across much more of the globe than the previous radiative anomalies and in general are more heterogeneous. On average, these anomalies lead to a global warming of around 0.02K in the most absorbing case (Figure 4a) or lead to a global cooling of around −0.07K in the most scattering case (Figure 4f). However, some of the largest surface air temperature anomalies are still centered on North Africa and the Tropical Atlantic Ocean.

Looking first at North Africa, we observe a tripole-like feature where the WAM region and much of Mediterranean coastline are out of phase with the central Sahara desert. In the most absorbing optical regime (Figure 4a), this takes the form of negative anomalies over −1K across the WAM region, Sahel, and Mediterranean Basin with a weaker positive anomaly up to 0.25K covering the rest of North Africa. As we increase the amount of scattering, this anomaly pattern slowly changes sign until the 0.1×0.9hem and 0.1×0.9hem (fixed LW) regimes where there is a positive anomaly of around 0.25K in the WAM region and a negative anomaly, peaking near −1K, across much of the Sahara desert (Figures 4e and 4f). These responses were investigated by Strong et al. (2015) and explained in part by changes to the evaporative flux over this region from associated dust-induced precipitation anomalies.

Across the tropical North Atlantic Ocean, we see a negative surface air temperature anomaly in all optical regimes, reaching up to −1K in the V&P and 0.1 × 0.9hem (fixed LW) optical regimes. This is due in large part to the decreased radiative flux from the attenuation by dust and emphasized by the largest temperature anomalies occurring in the most absorbing and most scattering regimes. However, in nearly all cases there is also a slight warming of the surface air temperature to the east of the North American continent in addition to a similar pattern across the western North Pacific, albeit of opposite sign. These anomalies could be indicative of larger-scale circulation features such as a shifting of the jet stream in these principal storm tracks.

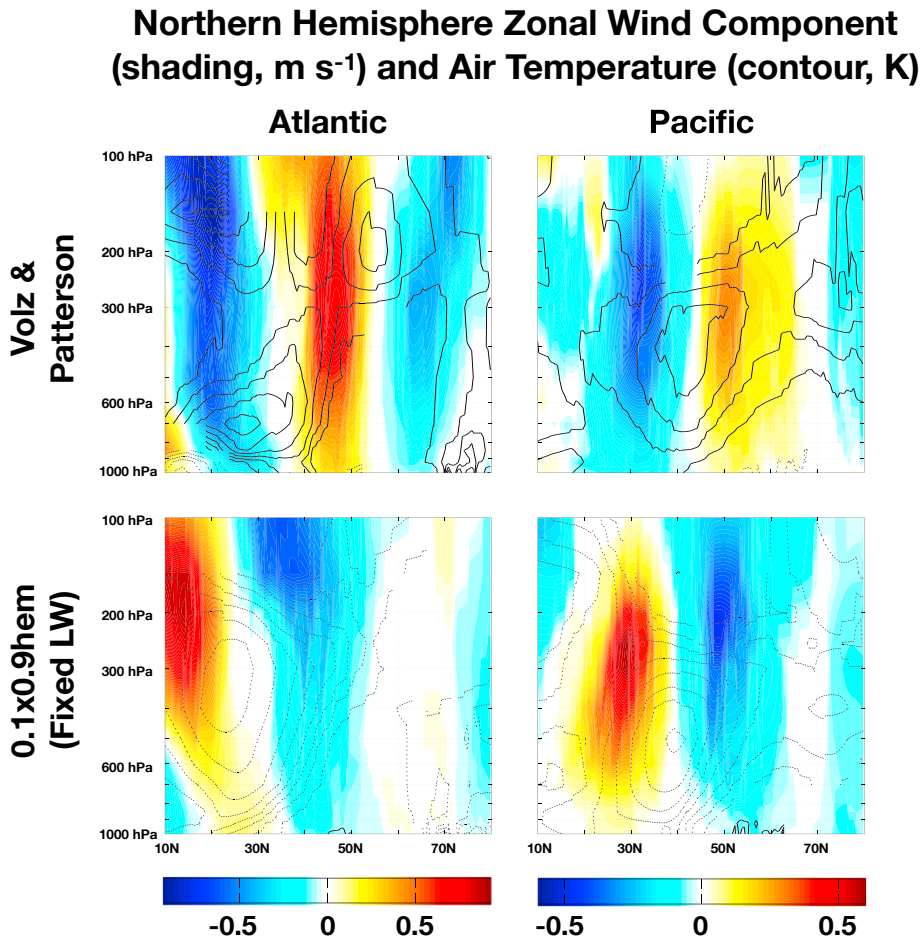

Figure 5. The Saharan dust–induced zonally averaged anomalies in the Northern Hemisphere zonal circulation. The shading shows the zonal wind component anomalies (m/s) and the contours show the air temperature anomalies (K, intervals of 0.05 K). The values are averaged over June–November and only those values that pass a Student's *t* test to 95% are shaded. The columns, from left to right, show the anomalies averaged over the Atlantic Basin (80W–0W) and Pacific Basin (120E–120W). The rows, from top to bottom, show the response in the V&P and 0.1 × 0.9hem (fixed longwave [LW]) optical regimes.

Looking at the zonal structure of these Northern Hemisphere regions in our most extreme cases, we do indeed see noticeable shifts in the jets (Figure 5). Plotted alongside air temperature anomalies, the zonal wind component follows the thermal wind relationship for much of the regions between 10N and about 50N. In the V&P case the anomalies westerlies in both the Atlantic and Pacific lay over the regions of increased gradient in equator-to-pole surface temperature (40N–50N). Meanwhile, the anomalous equatorial easterlies in the Atlantic occur over a region of surface cooling from the added dust plume (10N–30N), while those in the Pacific occur over a region of anomalous surface warming (20N–40N). Together, these anomalies are all centered on low- to middle-tropospheric warm anomalies.

Conversely, in the 0.1 × 0.9hem (fixed LW) case, the anomalous midlatitude easterlies overlay regions of decreased gradient in equator-to-pole surface temperature for both the Atlantic (30N–50N) and Pacific (40N–60N) Basins. Simultaneously, the subtropical anomalous westerlies occur over regions of decreased surface temperature for both basins. Again, these anomalies are centered on midtropospheric cool anomalies, in proper balance with the thermal wind relationship.

3.4. Precipitation Anomalies

The simulated precipitation anomalies due to an increase in Saharan-born dust (Figures 4g–4l and Table S1, fourth column) are again much more heterogeneous than the previous anomalies. While unsurprisingly most of the precipitation anomalies appear to be focused in the tropics, the lack of a significant globally averaged

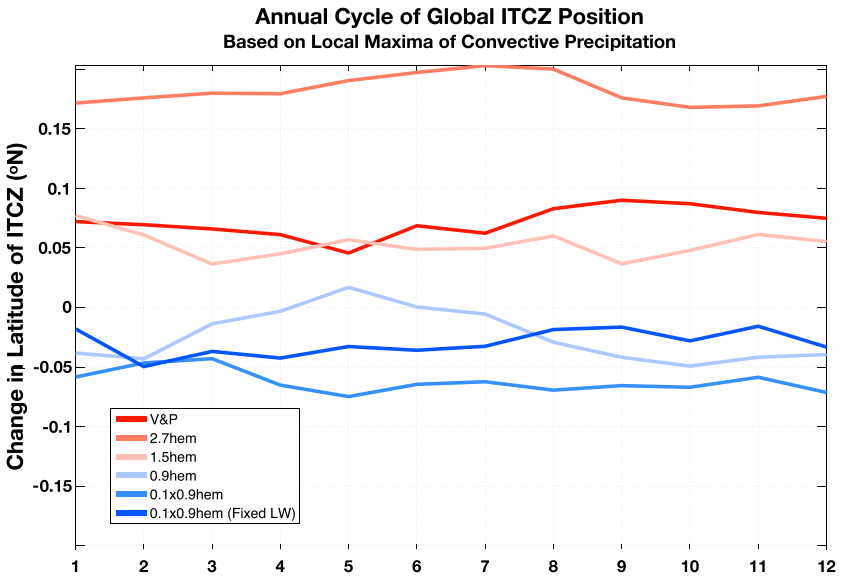

Figure 6. The Saharan dust–induced zonally averaged, latitudinal anomalies in the position of the Intertropical Convergence Zone (ITCZ), as defined by the latitudinal maxima in convective precipitation over the ocean. The shading of each line represents the relative scattering of dust in each optical regime with warmer colors representing less scattering dust and cooler colors representing more scattering dust. LW = longwave.

change in precipitation suggests a regional balance of total precipitation. When taken as a whole, it appears that more absorbing dust causes an increase in tropical precipitation in the Northern Hemisphere and a decrease in the Southern Hemisphere while more scattering dust causes a decrease in Northern Hemisphere tropical precipitation and an increase in Southern Hemisphere precipitation. While the response under the dust plume is also due to a local convective changes (Strong et al., 2015), these global equator-centric anomalies could be due to larger-scale changes in the location of the Intertropical Convergence Zone (ITCZ) (Wilcox et al., 2010; Woodage & Woodward, 2014) as it follows the warmer hemisphere. In fact when tracking the annual position of the ITCZ, as defined by the zonally averaged latitudinal maxima in convective precipitation over the oceans (Figure 6), we see that for absorbing dust the global ITCZ shifts northward across all months while for the more scattering dust regimes the ITCZ shifts generally southward. Interestingly, the largest responses do not occur in the most absorbing or scattering regimes.

The largest regional changes occur in the area of the WAM and have been the subject of multiple studies (Mahajan et al., 2012; Miller et al., 2004; Solmon et al., 2012; Strong et al., 2015; Yoshioka et al., 2007). Here we observe in the most absorbing optical regimes (Figures 4g–4i) that we get a general increase in the precipitation across the WAM region, up to 2.5 mm/day in the V&P case. However, as we increase the scattering properties of the dust, we drastically change the sign of this response to negative in the 0.1 × 0.9hem and 0.1 × 0.9hem (Fixed LW) regimes, exceeding −1.5 mm/day (Figures 4k and 4l). These anomalies can feed onto the strength or weakness of the WAM, respectively.

Moving to the Tropical Atlantic Ocean, we observe a significantly negative precipitation anomaly in every optical regime, with various spatial patterns. In the most absorbing V&P and 2.7hem cases there is a strong negative anomaly focused on the Western Atlantic Ocean and Caribbean Sea with anomalies up to −4 mm/day across Central America (Figures 4g and 4h). This negative anomaly stretches north into the Central Atlantic Basin and slightly south of the equator, enveloping the weaker positive eastern Atlantic and Gulf of Guinea precipitation anomalies. As the scattering of dust increases, the pattern begins to shift such that there is a negative anomaly along the southern border of the dust plume, extending from West Africa to the Lesser Antilles, abutting a positive anomaly extending from South America (Figures 4j–4l). These summertime precipitation anomalies can be indicative of changes to major tropical ocean precipitating systems such as tropical cyclones.

Of final note, we observe that the Indian subcontinent has significant changes to its simulated precipitation. In the most absorbing regimes there is a net increase in precipitation of almost 2 mm/day (Figures 4g and 4h), while in the most scattering cases there is a net decrease of up to −1 mm/day (Figures 4k and 4l). These anomalies could be indicative of changes to the Indian monsoon system and would have significant impact on any circulation features in the region but are outside the main interest of this study.

4. Tropical Cyclone Anomalies

4.1. Simulated Anomalies

The global tropical cyclone genesis and track density anomalies due to an increase in Saharan-born dust, as determined by our TC tracking routine, are plotted in Figure 7 where the contours represent anomalies in genesis or track density while the shading represents the percent change as given by the formula:

$$\text{Percent Change} = \frac{2 \times (\text{Density}_{\text{Full Dust}} - \text{Density}_{\text{Reduced Dust}})}{\text{Density}_{\text{Full Dust}} + \text{Density}_{\text{Reduced Dust}}} \times 100\% \quad (1)$$

Similarly, the anomalous accumulated cyclone energy (ACE) for various basins is provided in Table S2 and is defined by the formula:

$$\text{ACE} = \sum_{TC=1}^{\infty} \sum_{t=1}^{\infty} v_{\text{max},TC}(t)^2 \quad (2)$$

where the first summation is over every storm in a given basin in a given season, the second summation is over the length of time a given storm is active, and $v_{\text{max},TC}(t)$ is the maximum sustained wind velocity of the active tropical-cyclone-like vortex at a given time (t) using 6-hourly data. Seasonal ACE is a useful measure of basin-wide tropical cyclone activity as it incorporates changes to storm quantity, storm intensity, and storm duration providing a qualitative measure of basin-wide total TC activity (Bell et al., 2000).

We observe that in our simulations an increase of Saharan-born dust has substantial impacts to the global TC climatology. In every optical regime, there is a significant decrease in North Atlantic TC genesis events with the strongest response in the most absorbing and most scattering cases (Figures 7a–7f). In the V&P optical regime, dust causes over 0.5 fewer storms per year, which is over 75% of the modeled climatology (Figure 7a). In the 0.1 × 0.9hem (Fixed LW) optical regime, dust causes a little over 0.25 fewer storms per year, which is around 50% of the model's climatology (Figure 7f). This effect is weakened in the more moderate optical regimes of 1.5hem and 0.9hem where there are less than 0.25 fewer storms per year and only about a 20% change from the model's climatology (Figures 7c and 7d). These anomalies are primarily focused in the main development region (MDR) of the North Atlantic, between 10°N–25°N and 80°W–20°W, with an emphasis towards its easternmost boundary.

The genesis anomalies translate to decreased TC activity across the North Atlantic where again, we have the largest changes in the most absorbing and most scattering optical regimes (Figures 7g–7l). There are anomalies up to −2 storm days per year in the MDR for the V&P regime, which is over 75% of the climatology in that region, and additional negative anomalies, which overlay the traditional northwestward track of most Cape Verde style storms up to the southeastern United States (Figure 7g). Interestingly, while the negative anomalies in the 0.1 × 0.9hem (fixed LW) regime are of comparable magnitude, the peak anomalies appear to be shifted farther west from North Africa than the previous example but still maintain a similar westward extent (Figure 7l). And again, the weakened impact of the 1.5hem and 0.9hem dust means there is a weakened response in the TC track density (Figures 7i and 7j). These results are corroborated by the anomalies in ACE (Table S2), which show a significant decrease in tropical cyclone activity for each optical regime and with maximum anomalies occurring in the V&P regime.

Surprisingly, there are also significant anomalies in other basins around the globe, particularly in the northern Pacific and Indian Oceans. Focusing first on the northeast Pacific Basin, we see a strong east/west dipole develop in the V&P regime with decreased activity directly off the west coast of Central America amounting to over 0.25 less storms per year and over 1.5 less storm days per year (Figures 7a and 7g). These anomalies are balanced by those just west of 240°E and into the central North Pacific Basin where we see anomalies exceeding 0.25 more storms per year and over 1.5 more storm days per year, in a band focused tightly around 15°N. However, the spatial scale of the positive anomalies far outweighs that of the negative anomalies,

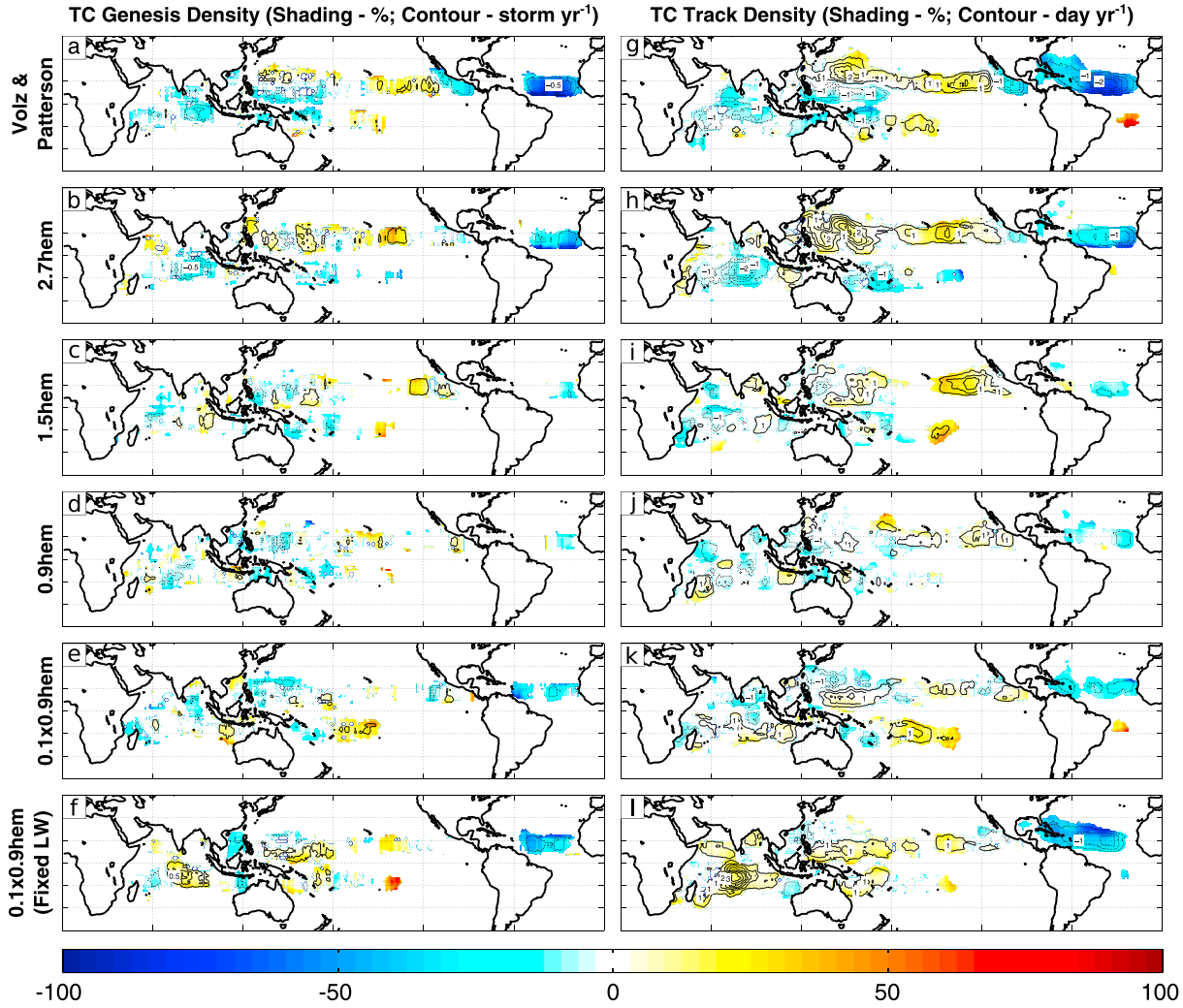

Figure 7. The TC genesis and lifetime-track density anomalies due to an increase in Saharan dust, comparable to the observed changes between the 1960s and 1980s, with differing optical properties. The shading denotes the percent change while the contours represent the absolute anomaly with a contour interval of 0.25 storm per year for TC genesis density and 0.5 day per year for TC track density. The values are indicative of changes over a 10° × 10° grid centered on each grid cell, and only those values with absolute magnitude larger than 0.1 storm per year for TC genesis density or 0.25 day per year for TC track density are shaded. The left column shows the TC genesis density anomalies (storms spawned per year), while the right column shows the TC lifetime-track density anomalies (days with storm present per year). The rows, from top to bottom, show the response in the V&P, 2.7hem, 1.5hem, 0.9hem, 0.1 × 0.9hem, and 0.1 × 0.9hem (fixed longwave [LW]) optical regimes and are ordered by increased scattering of dust.

leading to a net increase in TC activity as measured by ACE (Table S2). The density anomalies slowly decrease in magnitude as we transition to more scattering optical regimes with the far eastern negative anomalies decreasing by the 1.5hem optical regime, allowing for the largest increase in basin-wide TC activity as measured by ACE (Figures 7c and 7i and Table S2). Unlike in the North Atlantic, the largest and most homogeneous anomalies exist in only the most absorbing dust cases. While we get positive track density anomalies above 1 more storm day per year in the 0.1 × 0.9hem (fixed LW) case (Figure 7l), the overall pattern is much more heterogeneous than in the V&P, 2.7hem, and 1.5hem cases.

In the northwestern Pacific Basin our simulations show an interesting trend in TC activity. Despite TC genesis density anomalies never exceeding ±0.5 storms per year, we note some of the largest global anomalies in TC track density, indicating a change primarily in storm lifetime and not storm occurrence. In both the V&P and 2.7hem optical regimes values can exceed 2 more storm days per year (Figures 7g and 7h). There is also an interesting spatial pattern that develops as we transition to more scattering regimes. In the V&P dust case, there is a large north/south gradient in TC track density anomalies with negative anomalies generally between 15°S–15°N and positive anomalies generally north of 15°N, signifying a potential shift in TC activity northward

into the subtropical Northern Hemisphere (Figure 7g). This spatial pattern flips signs by the 0.1 × 0.9hem and 0.1 × 0.9hem (fixed LW) cases where there are now positive anomalies generally between 15°S and 15°N and negative anomalies generally north of 15°N, although these are weaker in the 0.1 × 0.9hem (fixed LW) case, potentially implying a shift of TC activity into the deep tropics and toward the south (Figures 7k and 7l).

Lastly, in the Indian Ocean we note relatively large changes in TC genesis density as well as TC track density, primarily in the most extreme optical regimes with absolute maximum values centered in the region between 0°S–15°S and 60°E–100°E. Again, there is an interesting transition as we move from more absorbing to more scattering dust. For the most absorbing dust cases we get a significant decrease of −0.5 storms per year and upward of −2 storm days per year (Figures 7g and 7h) in parts of the basin. But as we move to the 0.1 × 0.9hem and 0.1 × 0.9hem (fixed LW) regimes, we get significant increases of over 0.5 storms per year and well over 3.5 storm days per year in these same areas (Figures 7k and 7l). When taken together with the anomalies across the West Pacific, it appears as if there is a transition from shifting TC genesis and development to the north in the most absorbing cases (V&P and 2.7hem) and to the south in the most scattering cases (0.1 × 0.9hem and 0.1 × 0.9hem [fixed LW]). It is important to note that while some of these absolute anomalies in the northern Pacific and Indian Oceans are on the order of or larger than those in the North Atlantic, they represent only a small percentage change from the model's climatology, usually at most around 25%.

4.2. Comparison to Observations

As was stated in the methodology section, our choice of dust atmospheric loading climatology was influenced by the period of low dust transport away from the Sahara in the late 1960s compared with the period of high dust transport in the mid-1980s through early 1990s as measured at Barbados (Prospero & Lamb, 2003). These two periods represent the extremes in the direct observational record and as such presented a rich opportunity for a sensitivity study. While not an exact comparison, our simulations can be viewed as idealizations of the climate state in these two periods and thus lead us to compare our modeled TC anomalies with those of the real world.

We collect the observed TC record from the International Best Track Archive for Climate Stewardship data set (Schreck et al., 2014) and calculate the percent change from the 5-year periods 1965–1970 and 1983–1988, periods roughly centered on the maximum and minimum dust transport over Barbados in the observational record (Prospero & Lamb, 2003). These results are compared with the total percent change between the 200-year full and reduced dust simulations for each optical regime and presented in Figure 8.

While incorrect for much of the Pacific Basin, the most striking comparison occurs in the North Atlantic where our simulated TC anomalies explain between 10% and 150% (depending on the optical properties of the dust) of the observed trend of 30% fewer storm days per year. Interestingly, the most similar percent difference occurs in our most artificial optical regime of 0.1 × 0.9hem (fixed LW), while the optical regimes regarded as most accurate of Saharan dust, V&P and 2.7hem, either over or under estimate the observed trend, respectively. A possible explanation of this result may be due to the mixing of dust aerosols with purely scattering aerosols such as sulfate or nitrate. It has been shown that the extinction efficiency of dust decreases from observations as ammonia concentrations increase (Ginoux, Clarisse, et al., 2012)

As to be expected, the more middle-of-the-road optical regimes of 1.5hem and 0.9hem display minimal percent changes when compared with the observations as they were also the simulations with the smallest climate perturbations. On the whole, however, every optical regime simulates a negative trend in TC activity across the North Atlantic as was observed between the late 1960s and mid-1980s.

Other basins around the world do not share the same relationship between our simulations and the observed trend. In the northeast Pacific Basin, our simulations show an increase in TC activity anywhere between 3% and 7%, which is of the same sign as the observations but dwarfed by the substantial 40% increase in observed TC activity. This may indicate that while Sahara dust has a nonnegligible impact on northeastern Pacific TCs, it is not the primary driving mechanism. Interestingly, the largest changes occur in the most intermediate of optical properties, 2.7hem, 1.5hem, and 0.9hem. Meanwhile, in the northwestern Pacific our simulations have the complete opposite sign from the observed trend in every optical range, which was originally expected considering the distance between the forcing and response regions.

Lastly, in the Southern Hemisphere the observations of both the South Pacific and Indian Oceans show a general increase in TC activity. Meanwhile, our simulations show a common pattern of decreasing TC activity for the most absorbing optical regimes and increasing TC activity for the most scattering optical regimes,

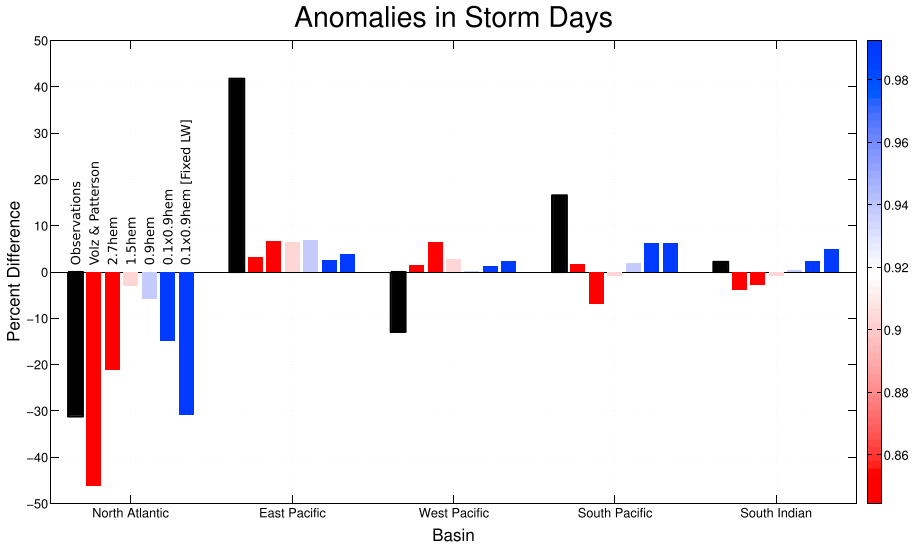

Figure 8. A comparison between the observed anomalies in total TC activity and the simulated anomalies due to an increase in Saharan dust, comparable to the observed changes between the 1960s and 1980s, with differing optical properties across several basins. The observations are drawn from the IBTrACS data set (Schreck et al., 2014) and calculated as the percent difference between the periods 1960–1965 and 1983–1988 for each basin. Each bar represents the percent difference in total TC activity across individual basins with the shading representing the single scattering albedo of 1 μm dust at 550 nm of each optical regime. The bars, from left to right, show the response in the observations and V&P, 2.7hem, 1.5hem, 0.9hem, 0.1 × 0.9hem, and 0.1 × 0.9hem (fixed LW) optical regimes and are ordered by increased scattering of dust. IBTrACS = International Best Track Archive for Climate Stewardship; LW = longwave.

with the obvious exclusion of the V&P dust case in the South Pacific. This means that the closest our simulations get to representing the observed trend in Southern Hemisphere TC activity is in the 0.1 × 0.9hem and 0.1 × 0.9hem (fixed LW) regimes. In fact, the 0.1 × 0.9hem case in the Indian Ocean is the closest to resolving the actual observed trend, which again may be explained by the decreased extinction efficiency of dust aerosols when mixed with purely scattering aerosols, a trait not accounted for in these simulations.

5. Impact of Dust on Tropical Cyclone-Related Parameters

Understanding what drives changes in individual tropical cyclones, let alone their basin-wide climatologies, is a monumental task and the subject of numerous prior studies. Much of this research has pointed toward the influencing effects of low-level vorticity, vertical wind shear, midlevel vertical velocity, midlevel moisture, and sea surface temperature anomalies. In addition, several other quantities have shown utility in TC development prediction such as the presence of convective precipitating systems as well as upper ocean heat content, maximum potential surface wind speed, surface to midlevel entropy deficit, and lower-level atmospheric thermal structure anomalies.

These metrics have been compiled into empirically derived formulations of the likelihood for a tropical storm to develop given the local conditions, called genesis potential indices (GPIs). In addition to examining the individual metrics, we will also explore the GPIs developed by Emanuel and Nolan (2004), Emanuel (2010), Tippett et al. (2011), Gray (1979), and Royer et al. (1998). Hereafter, these will be referred to as EN04, E10, T11, G79, and R98, respectively. To focus on the regions in which our model simulates tropical cyclogenesis, we follow the protocol of Held and Zhao (2011) and genesis weight the GPIs and metrics using the formula:

$$[M(x,y)]_G = \frac{\overline{G(x,y)M(x,y)}}{\overline{G(x,y)}} \tag{3}$$

where $M(x,y)$ is the spatial map of monthly means of the metric of choice, $G(x,y)$ is the spatial map of monthly means of the genesis density for the reduced dust simulation, and the overline is an average over the 12 months. As these GPIs are point forecast formulas and we are interested in more regional scale changes,

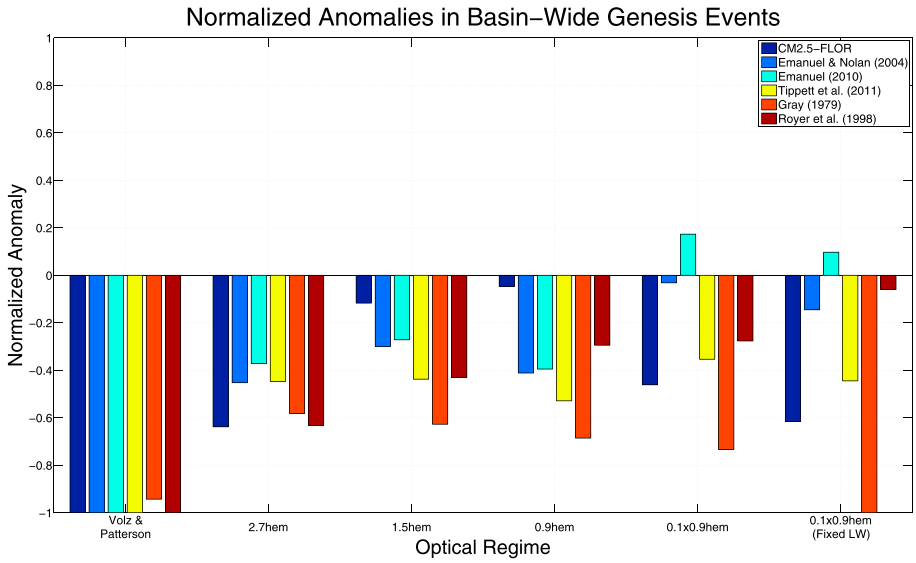

Figure 9. A comparison between the simulated anomalies in North Atlantic TC genesis events and the simulated anomalies in genesis potential indices due to an increase in Saharan dust, comparable to the observed changes between the 1960s and 1980s, with differing optical properties across several basins. Each bar represents the basin-averaged anomalies in TC genesis events from the tropical cyclone tracking scheme or as predicted from several genesis-weighted genesis potential indices. The bars, from left to right, show the response in the TC tracking scheme and as predicted from the genesis potential indices of Emanuel and Nolan (2004), Emanuel (2010), Tippett et al. (2011), Gray (1979), and Royer et al. (1998). Each set of bars is normalized by its maximum absolute value across the six dust optical regimes. CM2.5-FLOR = CM2.5 Forecast-oriented Low Ocean Resolution version.

we average over each individual basin and compare them to the results from our TC tracking routine. Our goal is to find a basin-wide explanation for each basin's simulated tropical cyclone anomaly rather than focus on subregions of individual basins.

5.1. North Atlantic

We begin in the North Atlantic by calculating the basin average of the genesis-weighted GPI anomalies (Figure 9). Our aim is to find an index that not only is the same sign as the simulated TC genesis density anomalies but also get the relative magnitudes between optical regimes correct, namely, the largest anomalies in the most absorbing and most scattering regimes and the smallest anomalies in the middle-of-the-road regimes. To this end, we normalize the anomalies of each index by their absolute maximum values across the optical regimes.

We note that, save for two instances of the E10 index in the most scattering regimes, all GPIs predict a decrease in North Atlantic tropical cyclone activity. Similarly, all but the G79 index predict the largest decrease in basin-wide TC activity in the V&P optical regime. However, none of the common GPIs are able to predict the simulated pattern of largest decreases occurring in the V&P and 0.1 × 0.9hem (Fixed LW) regimes while simultaneously lowest in the most moderate of optical regimes. The closest is the G79 index; however, it is monotonically decreasing as the scattering by dust increases from 2.7hem to 0.1×0.9hem regimes. Instead, we must turn to each of the individual TC development parameters mentioned above, which the basin-averaged, genesis-weighted values are listed along side the basin-averaged TC track density anomalies in Table S3. Our goal with this analysis is to find a parameter that has a sign consistent with what is expected from the literature for a given change in TC activity across all optical property regimes (e.g., increased TC activity generally occurs with increased sea surface temperatures, not the opposite) and whose relative magnitude across the optical regimes is the same as the relative magnitudes of the TC track density anomalies (e.g., the largest change in TC activity should occur in the same optical regime as the largest change in the TC development parameters and vice versa).

For the purely dynamics-related variables (Table S3), given a decrease in tropical cyclone activity, we should expect a decrease in absolute vorticity anomalies as well as an increase in vertical wind shear. However, we see that neither of these parameters consistently have the correct sign given the simulated basin-wide TC

anomalies across optical property regimes. This is further emphasized at the local level (Figure S2, first and second columns) where, even though the largest changes occur in the tropical North Atlantic, the patterns largely flip sign as dust goes from more absorbing to more scattering, which in turn leads to inconsistent comparisons with the simulated TC density anomalies. Conversely, the midlevel vertical pressure velocity, which should increase for a given decrease in TC activity as suggested by Held and Zhao (2011), does in fact have the correct sign across all optical regimes. However, the vertical velocity values are monotonically decreasing with increasing scattering, which is not in line with the pattern of TC density anomalies. At the local level, this is evidenced by large-scale, and fairly strong, subsidence anomalies across the North Atlantic in the V&P case, which decrease in extent and magnitude with increasing scattering by dust (Figure S2, third column). These same issues with consistent trends also arise in the moisture (Figure S3) and vertically integrated quantities (Figure S5) where we should expect general midlevel drying, decreased convective rainfall, decreased maximum potential wind speed, increased entropy deficit, and decreased gradient of equivalent potential temperature for a given decrease in TC activity with the largest anomalies in the most absorbing and scattering cases.

Interestingly, the most consistent set of variables are the temperature-related relative sea surface temperature and upper ocean heat content (Figure S4), which, for a given decrease in TC activity, should be expected to decrease in tandem. Both get the correct sign of anomalies to match those expected from the TC density anomalies, but the relative magnitudes between the 0.9hem and 0.1×0.9hem cases cause an exception. This may suggest a strong ocean influence on Atlantic TC variability as suggested by Wang et al. (2012).

As none of the common TC development parameters can consistently explain the anomalies we see in TC track density across the North Atlantic, we must search for another answer. Dust's impact to climate is highly dependent on its ToA net radiative flux anomaly (Miller et al., 2014). This would suggest that if we compare dust's ToA radiative perturbation with the basin-averaged TC statistics, we may find a possible relationship. To narrow in on the predictive behavior of this relationship, we calculate dust's LW and SW radiative flux anomaly over the North Atlantic MDR and plot it against the basin-wide ACE anomalies for each optical regime (Figure 10).

What we observe is a strictly monotonic relationship between the net ToA radiative imbalance over the MDR and the ACE anomaly for the entire basin. The most scattering and most absorbing regimes cause the largest ToA radiative anomalies as well as have the largest ACE anomalies. Meanwhile, the more moderate optical regimes of 1.5hem and 0.9hem have the smallest ToA radiative flux anomalies in addition to the smallest ACE anomalies. This would appear to suggest that dust's radiative effects over the main TC-generating region of the North Atlantic affect the entire TC climatology of the basin. It also appears that the basin-wide ACE anomalies also show the most sensitivity to the ToA longwave anomalies in the most scattering cases and the most sensitivity to the ToA shortwave anomalies in the most absorbing cases.

5.2. Northeast and Central Pacific

While our original focus was on the impacts across the North Atlantic Basin, the simulated anomalies across the Indo-Pacific Basins demand an investigation. Despite their apparent disagreement with the observations, we may be able to glean information about the larger-scale impact of dust on the tropics. A full examination of this would require a separate study, so we will only provide a brief overview of some possible explanations here. Looking first at the northeast Pacific, we again look at the aforementioned TC development parameters averaged across the basin and compare them to the basin-averaged TC track density anomalies (Table S4).

In the northeast Pacific, the TC track density anomalies are all positive and actually largest for the more moderate optical regimes of 2.7hem, 1.5hem, and 0.9hem. As was common in the North Atlantic, no one basin-averaged parameter consistently explains the simulated basin-wide TC track density anomalies, and in fact each variable has the wrong sign at least once for each optical regime. However, it appears that the vertical shear (Figure S3, second column), midlevel vertical velocity (Figure S3, third column) and relative sea surface temperature (Figure S4, first column) come closest to the simulated TC track density anomalies. This can be seen at the regional level where in the V&P case we have strong shear and subsidence along the Central American coastline and weakened shear, general ascent, and surface warming in the central Pacific, which becomes more insignificant with increasing scattering by dust. This perhaps suggests a nonlocal atmospheric bridge-type response reminiscent of Ham et al. (2013) and Kucharski et al. (2015).

In this situation, the drastic cooling of the North Atlantic in the spring months leads to a central Pacific ENSO-like state the following fall by setting up a low-level anticyclonic circulation across Central America

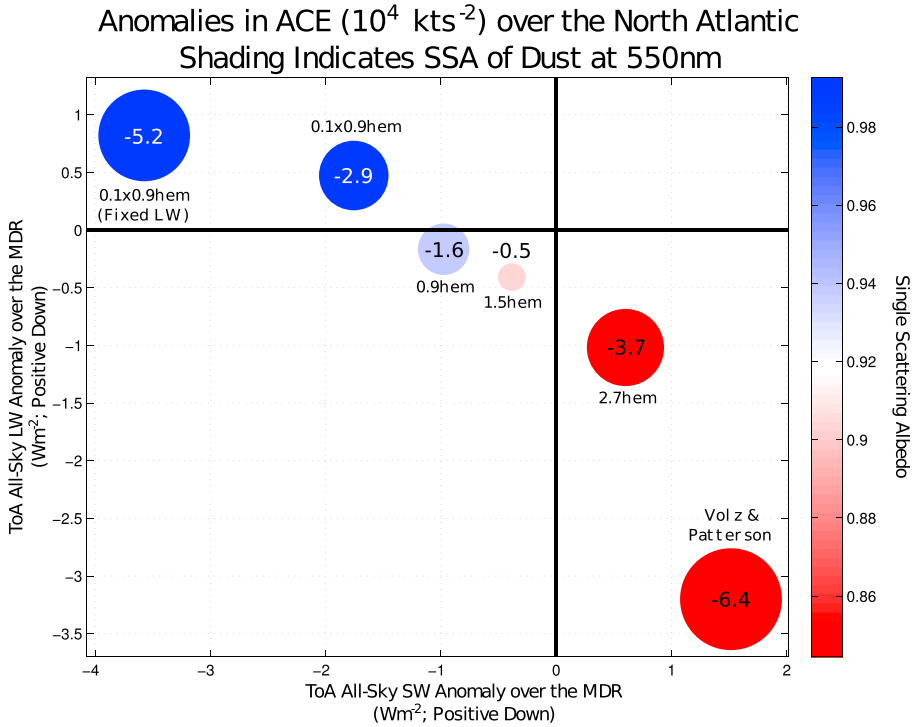

Figure 10. The accumulated cyclone energy anomalies across the North Atlantic due to an increase in Saharan dust, comparable to the observed changes between the 1960s and 1980s, with differing optical properties. The *x* axis is the top of atmosphere shortwave anomaly (positive downwards; W/m^2) averaged across the North Atlantic main development region, while the *y* axis is the top of atmosphere longwave anomaly (positive downwards; W/m^2) averaged across the North Atlantic main development region. The size of each circle represents the North Atlantic basin-averaged accumulated cyclone energy anomaly for each optical regime with each number being the exact value (10^4 kts^{-2}). The shading of each circle represents the single scattering albedo of 1-μm dust at 550 nm of each optical regime. ACE = accumulated cyclone energy; MDR = main development region; ToA = top of the atmosphere; SSA = Single Scattering Albedo.

and a cyclonic circulation over the central to western Pacific Ocean. As the largest TC density anomalies are in the V&P and 0.1 × 0.9hem (Fixed LW) regimes, we examine the potential for this type of nonlocal response in those two regimes (Figure 11).

In the V&P case, we see the strong relative cooling of the tropical North Atlantic Ocean across all seasons. There is a semipermanent cyclonic circulation that sets up off the coast of Northwest Africa. Across the northeastern Pacific there are easterly winds reaching west of Central America, which are strongest in the boreal summer months and a weaker cyclonic circulation in the central Pacific, which is strongest in the boreal spring and summer months. These wind anomalies would lead to a central Pacific ENSO-like state, which is associated with TC density anomalies in the central Pacific and decreased amounts off the western Central American coastline (Kim et al., 2011).

In the 0.1 × 0.9hem (fixed LW) case, there is again persistent surface cooling across much of the tropical North Atlantic but instead a semipersistent anticyclonic circulation off the coast of Northwest Africa and almost no surface anomalies across the tropical North Pacific Ocean. Thus, the atmospheric bridge hypothesis does not seem to be as accurate for the most scattering regimes, possibly due to a general atmospheric cooling response as shown by Strong et al. (2015), which may offset any increase in convective activity.

5.3. Northwest Pacific and Indian

Finally, transitioning to the Indo-Pacific Basins, we once again calculate individual basin-averaged TC parameters (Tables S5 and S6). Focusing first on the northwest Pacific Basin, there is even more disagreement between the listed parameters and the TC track density anomalies. No single parameter is able to capture the large increase in TC track density for the 2.7hem case and the lowest values for the 0.9hem and 0.1 × 0.9hem cases while simultaneously capturing the correct sign of the anomalies. Although on a regional scale, the low-level absolute vorticity (Figure S2, first column) in the most absorbing and scattering cases does seem to come

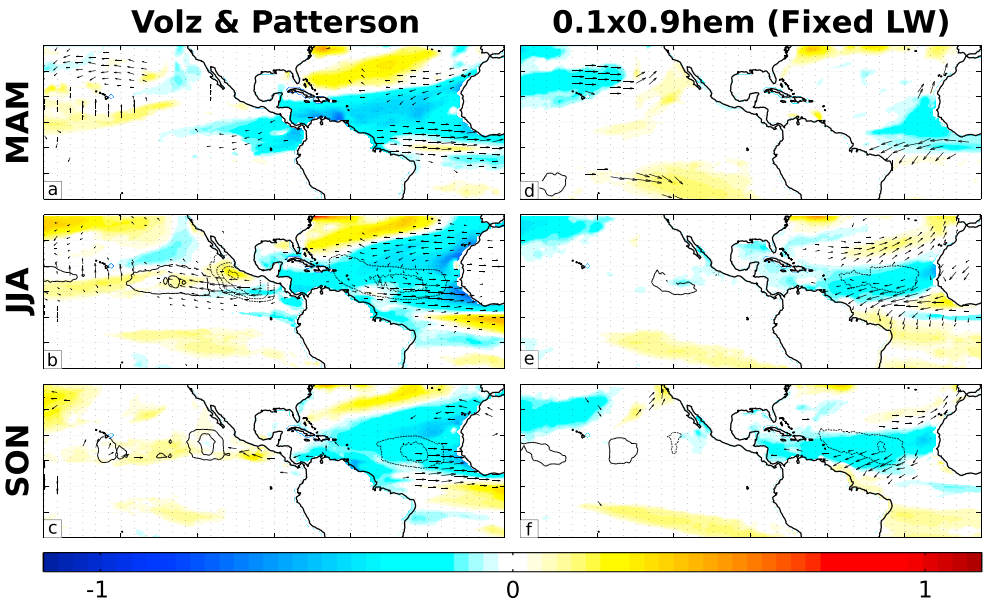

Figure 11. The Saharan dust–induced anomalies across the North Atlantic and northeast Pacific Basins during boreal spring, summer, and fall seasons. The shading represents tropical relative sea surface temperature anomalies (K), the vector arrows represent the 2-m reference level wind anomalies (m/s), and the contours represent TC lifetime-track density as described in Figure 7. The left column shows the seasonal anomalies in the Volz & Patterson optical regime, while the right column shows the seasonal anomalies in the 0.1 × 0.9hem (fixed longwave [LW]) optical regime. From top to bottom, the rows display the March-April-May (MAM), June-July-August (JJA), and September-October-November (SON) anomalies, respectively.

closer to the regional patterns of TC density anomalies with a north-south seesaw in the tropical northwest Pacific. Meanwhile, in the South Indian Basin there are two potential candidates, namely, the vertical wind shear and the convective precipitation. While both do not perfectly match the pattern of a generally increasing level of TC activity or show similar patterns at a local level to the simulated TC density anomalies (Figure S2, first column and Figure S3, second column), they do consistently get the signs correct and could suggest a larger-scale atmospheric-based mechanism, perhaps one which could also explain the anomalies in the northwest Pacific Basin.

Looking for nonlocal explanations of the simulated TC track density anomalies, we again return to Figure 7 and note that while focusing on the Indo-Pacific region, it appears that there is a general shift of TC activity from the north in the most absorbing cases to the south in the most scattering cases. For the V&P optical regime, this means an increased level of TC activity to the North in the Northern Hemisphere and decreased activity through the equator and into the Southern Hemisphere. However, as we increase the level of scattering, this trend reverses and instead we have increased convective activity in the Southern Hemisphere and decreased activity farther to the north. This may be due to the substantial heating or cooling we are imposing with our Saharan dust perturbations, respectively, affecting the general hemispheric energy balance and associated circulation features.

We calculate the dust-induced anomalies in the zonally averaged meridional heat transport by both the atmosphere and ocean (Figure 12) and indeed see a reversal in cross-equatorial heat transport between the most absorbing and most scattering dust optical regimes. For the most absorbing dust regimes, there is a strong southward transport of heat out of the Northern Hemisphere deep tropics from about 0° – 10°N, split approximately equally between atmosphere and ocean components. The atmosphere component would indicate an increase in Northern Hemisphere tropical convection to initialize this heat transport. In the most scattering regimes, there is a strong cross-equatorial heat transport into the Northern Hemisphere tropics. This would need to be offset by an increase in Southern Hemisphere tropical convection. These anomalies would lead to a shift in the main convecting regions, and thus opportunities to generate tropical cyclones, into the relatively warmer hemisphere. In general, this also tracks the position of the ITCZ, and the meridional heat transport anomalies here are in line with the changes we saw in Figure 6. They additionally manifest themselves in the far-field simulated changes to TC density across the Indo-Pacific Basins.

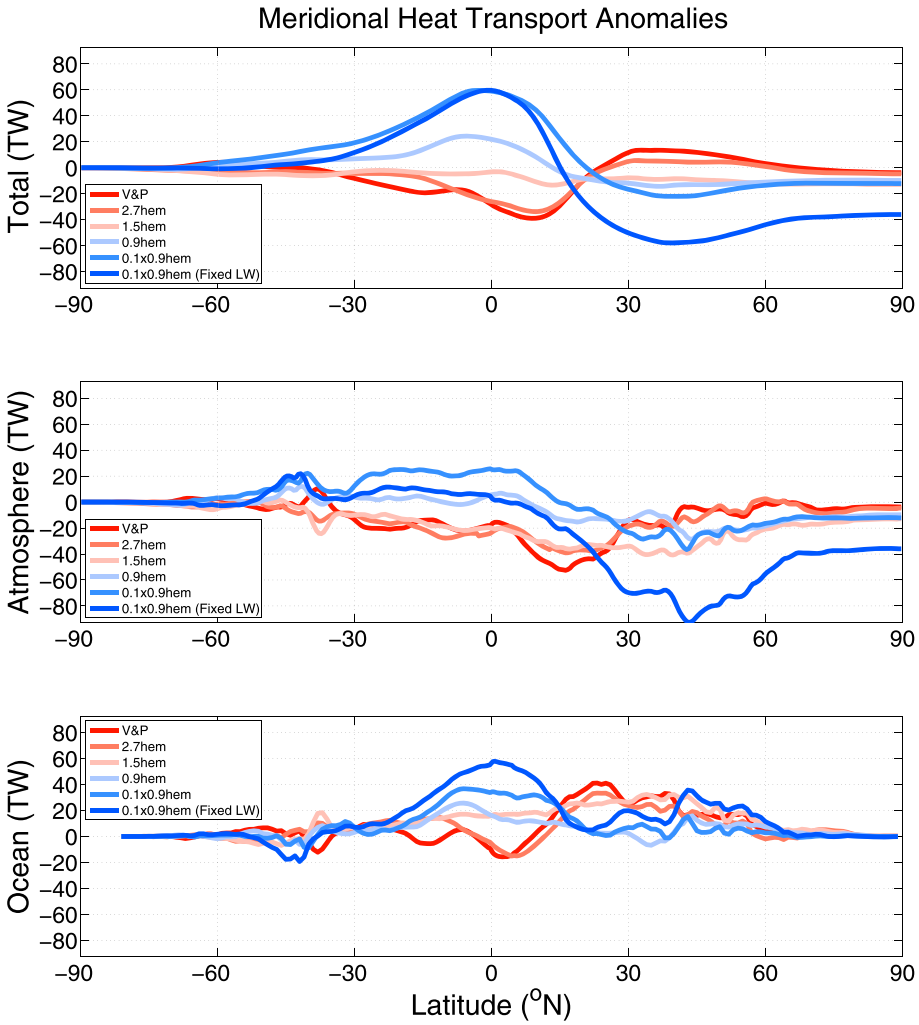

Figure 12. The Saharan dust–induced zonally averaged, meridional heat transport anomalies. From top to bottom, the rows show the total, atmosphere-only, and ocean-only meridional heat transport anomalies, respectively, in units of terrawatts (TW). The shading of each line represents the relative scattering of dust in each optical regime with warmer colors representing less scattering dust and cooler colors representing more scattering dust.

6. Conclusions

Saharan dust accounts for one of the largest regional aerosol forcings in the world. Due to its climatological advection westward, dust can induce substantive direct interactions with the climate across the tropical North Atlantic. In particular, it can lead to significant anomalies in the North Atlantic's main development region for tropical cyclones and thus has the potential to alter North Atlantic hurricane statistics. We have explored this impact from a climate perspective using the fully coupled GFDL CM2.5-FLOR model using realistic variations in atmospheric burden of Saharan dust across a wide range of aerosol optical regimes.

We found that Saharan-born dust affects the climate state in a similar fashion to previous studies. There is a distinctly opposite response from our most absorbing regimes to our most scattering regimes in several common variables. The more absorbing dust leads to a net positive radiative flux anomaly at the ToA over North Africa, whereas the more scattering dust causes a net negative radiative flux anomaly at the ToA over North Africa. Saharan-born dust in all optical regimes causes a significant negative radiative flux over the North Atlantic at the ToA. In addition, due to the solar dimming effect of dust, all cases see a negative net radiative flux at the surface underneath the dust plume anomaly. These radiative anomalies lead either directly or indirectly to other global anomalies in surface air temperature and precipitation. And while many of these anomalies

are strongest in the area directly influenced by the dust plume, there are significantly large anomalies in other regions such as the equatorial Pacific and the Indian subcontinent.

We utilized a TC tracking scheme to determine how Saharan-born dust affects the climatological TC statistics in various basins of the world. As was predicted, we saw that Saharan-born dust causes a significant decrease in TC activity across the North Atlantic Basin in nearly every optical regime, to varying magnitudes. In comparison to observations over the period idealized by our model simulations, we found that our variations in Saharan dust could explain nearly all of the observed trend depending on the optical regime used. Simultaneously, there were unexpectedly large TC anomalies in nearly every other basin across the globe with some of the largest anomalies occurring in the West Pacific and Indian Oceans, albeit anomalies that only accounted for a small percentage of the model's natural climatology. The agreement with observations for these anomalies was less striking than those in the North Atlantic.

To understand these TC anomalies, we examined several common predictive variables for TC activity. Many of the most common GPI's failed to coherently predict TC changes in the North Atlantic. An examination of their constituent variables similarly led to inconclusive results. However, when considering other uncommon utilities, we found that there was a monotonic relationship between North Atlantic Basin–wide ACE anomalies and Saharan dust–induced ToA radiative anomalies across the MDR. In other basins of the world, we put forth several theories to explain the observed TC anomalies. In the East and central Pacific, we hypothesize that the simulated TC anomalies are due to the established linkage between East Pacific circulations and the North Atlantic whereby certain ENSO-like states are stimulated. Conversely, in the West Pacific and Indian Oceans, we theorize that the TC anomalies are due in part to large-scale hemispheric shifts of the primary zones of convective activity.

This study, while interesting in results, has a number of important limitations. First is the prescribed aerosol forcing, which neglects the aerosol-induced changes on dust emissions through varying surface winds and aridity, which can be an important feedback on the climate system. Similarly, the lack of a time-evolving aerosol atmospheric loading limits the ability to directly compare this study's results to observations. The model itself is limited both by dynamics and parameterizations. The resolution of CM2.5-FLOR is high enough to get a reasonable TC climatology but is not high enough to have a proper distribution of storm intensity, instead preferentially simulating weaker TCs. Additionally, the lack of including the aerosol indirect effect in the model limits the results of this study as dust-cloud microphysical interactions have the potential for redistributing energy within tropical cyclones, which could impact their duration and strength. Finally, while the inclusion of a fully dynamic ocean is novel for this study, the simulation time would have to be extended substantially to include any deeper ocean impacts, which may be of consequence for paleoclimate work.

Due to dust's regional mineralogical heterogeneity, it would be a worthwhile venture to explore how implementing several concurrent dust aerosols with differing optical properties in a single model simulation would affect our results. This could be initiated by studies focusing on how altering emissions of dust from various source subregions, rather than the entire Sahara, affects the climate state. Additionally, a more realistic historical simulation could help in the comparison of Saharan dust's impact on tropical cyclones to the observational record.

Our findings support several notions of Saharan-born dust's impact to the climate as well as illuminate some new global-scale impacts. They also reinforce the notion that dust's climate impact is highly dependent on the choice of optical regime, leading to nearly opposite climate states given the balance between a dust aerosol's absorption and scattering abilities. While a direct comparison to observations is not possible given the idealized nature of this work, our findings relating a modeled decrease in TC activity across the North Atlantic to a similar trend in the observational record has significant implications for future simulations and predictive work.

Acknowledgments
The model code for CM2.5-FLOR is freely available and can be downloaded at https://www.gfdl.noaa.gov/cm2-5-and-flor/. This report was prepared in part by Jeffrey Strong under award NA14OAR4320106 from the National Oceanic and Atmospheric Administration, U.S. Department of Commerce and in part by Gabriel Vecchi under award NA14OAR4830101 from the National Oceanic and Atmospheric Administration, U.S. Department of Commerce. The statements, findings, conclusions, and recommendations are those of the author(s) and do not necessarily reflect the views of the National Oceanic and Atmospheric Administration or the U.S. Department of Commerce.

References

Adams, A. M., Prospero, J. M., & Zhang, C. (2012). CALIPSO-derived three-dimensional structure of aerosol over the Atlantic basin and adjacent continents. *Journal of Climate*, *25*, 6862–6879. https://doi.org/10.1175/JCLI-D-11-00672.1

Anderson, J. L., Balaji, V., Broccoli, A. J., Cooke, W. F., Delworth, T. L., Dixon, K. W., et al. (2004). The new GFDL global atmosphere and land model AM2-LM2: Evaluation with prescribed SST simulations. *Journal of Climate*, *17*, 4641–4673. https://doi.org/10.1175/JCLI-3223.1

Balkanski, Y. J., Schulz, M., Claquin, T., & Guibert, S. (2007). Reevaluation of mineral aerosol radiative forcings suggests a better agreement with satellite and AERONET data. *Atmospheric Chemistry and Physics*, *7*, 81–95. https://doi.org/10.5194/acp-7-81-2007

Bell, G. D., Halpert, M. S., Schnell, R. C., Higgins, R. W., Lawrimore, J., Kousky, V. E., et al. (2000). The 1999 North Atlantic and eastern North Pacific hurricane seasons [in "Climate Assessment for 1999"]. *Bulletin of the American Meteorological Society*, *81*(6), S19–S22. https://doi.org/10.1175/1520-0477(2000)81[s1:CAF]2.0.CO;2

Braun, S. A. (2010). Reevaluating the role of the Saharan air layer in Atlantic tropical cyclogenesis and evolution. *Monthly Weather Review*, *138*, 2007–2037. https://doi.org/10.1175/2009MWR3135.1

Bretl, S., Reutter, P., Raible, C. C., Ferrachat, S., Poberaj, C. S., Revell, L. E., & Lohmann, U. (2015). The influence of absorbed solar radiation by Saharan dust on hurricane genesis. *Journal of Geophysical Research: Atmospheres*, *120*, 1902–1917. https://doi.org/10.1002/2014JD022441

Caquineau, S., Gaudichet, A., Gomes, L., & Legrand, M. (2006). Mineralogy of Saharan dust transported over northwestern Tropical Atlantic Ocean in relation to source regions. *Journal of Geophysical Research*, *107*, D154251. https://doi.org/10.1029/2000JD000247

Chavas, D. R., & Emanuel, K. A. (2010). A QuickSCAT climatology of tropical cyclone size. *Geophysical Research Letters*, *37*, L18816. https://doi.org/10.1029/2010GL044558

Colarco, P. R., Nowottnick, E. P., Randles, C. A., Yi, B., Yang, P., Kim, K.-M., et al. (2014). Impact of radiatively interactive dust aerosols in the NASA GEOS-5 climate model: Sensitivity to dust particle shape and refractive index. *Journal of Geophysical Research: Atmospheres*, *119*, 753–786. https://doi.org/10.1002/2013JD020046

DeMott, P. J., Sassen, K., Poellot, M. R., Baumgardner, D., Rogers, D. C., Brooks, S. D., et al. (2003). African dust aerosols as atmospheric ice nuclei. *Geophysical Research Letters*, *30*(14), 1732. https://doi.org/10.1029/2003GL017410

Delworth, T. L., Rosati, A., Anderson, W., Adcroft, A. J., Balaji, V., Benson, R., et al. (2012). Simulated climate and climate change in the GFDL CM2.5 high-resolution coupled climate model. *Journal of Climate*, *25*, 2755–2781. https://doi.org/10.1175/JCLI-D-11-00316.1

Donner, L. J., Wyman, B. L., Hemler, R. S., Horowitz, L. W., Ming, Y., Zhao, M., et al. (2011). The dynamical core, physical parameterizations, and basic simulation characteristics of the atmospheric component AM3 of the GFDL global coupled model CM3. *Journal of Climate*, *24*, 3484–3519. https://doi.org/10.1175/2011JCLI3955.1

Dunion, J. P., & Velden, C. S. (2004). The impact of the Saharan air layer on Atlantic tropical cyclone activity. *Bulletin of the American Meteorological Society*, *85*, 353–365. https://doi.org/10.1175/BAMS-85-3-353

Emanuel, K. A. (2010). Tropical cyclone activity downscaled from NOAA-CIRES reanalysis, 1908–1958. *Journal of Advances in Modeling Earth Systems*, *2*, 1–12. https://doi.org/10.3894/JAMES.2010.2.1

Emanuel, K. A., & Nolan, D. S. (2004). Tropical cyclone activity and global climate. In *26th Conference on Hurricanes and Tropical Meteorology* (pp. 240–241). Miami, FL: American Meteorological Society.

Evan, A. T., Dunion, J. P., Foley, J. A., Heidinger, A. K., & Velden, C. S. (2006). New evidence for a relationship between Atlantic tropical cyclone activity and African dust outbreaks. *Geophysical Research Letters*, *33*, L19813. https://doi.org/10.1029/2006GL026408

Gillette, D. A., Adams, J., Endo, A., Smith, D., & Kihl, R. (1980). Threshold velocities for input of soil particles into the air by desert soils. *Journal of Geophysical Research*, *85*, 5621–5630. https://doi.org/10.1029/JC085iC10p05621

Ginoux, P., Clarisse, L., Clerbaux, C., Coheur, P.-F., Dubovik, O., Hsu, N. C., & Damme, M. V. (2012). Mixing of dust and NH_3 observed globally over anthropogenic dust sources. *Atmospheric Chemistry and Physics*, *12*, 7351–7363. https://doi.org/10.5194/acp-12-7351-2012

Ginoux, P., Prospero, J. M., Gill, T. E., Hsu, N. C., & Zhao, M. (2012). Global-scale attribution of anthropogenic and natural dust sources and their emission rates based on MODIS Deep Blue aerosol products. *Reviews of Geophysics*, *50*, RG3005. https://doi.org/10.1029/2012RG000388

Gray, W. M. (1979). Hurricanes: Their formation, structure and likely role in the tropical circulation. In D. B. Shaw (Ed.), *Meteorology Over the Tropical Oceans* (pp. 155–218). James Glaisher House, Grenville Place, Bracknell, Berkshire: R. Meteor. Soc.

Grousset, F. E., Ginoux, P., Bory, A., & Biscaye, P. E. (2003). Case study of a Chinese dust plume reaching the French Alps. *Geophysical Research Letters*, *30*(6), 1277. https://doi.org/10.1029/2002GL016833

Ham, Y.-G., Kug, J.-S., Park, J.-Y., & Jin, F.-F. (2013). Sea surface temperature in the north tropical Atlantic as a trigger for El Niño/Southern Oscillation events. *Nature Geoscience*, *6*, 112–116. https://doi.org/10.1038/NGEO1686

Held, I. M., & Zhao, M. (2011). The response of tropical cyclone statistics to an increase in CO_2 with fixed sea surface temperatures. *Journal of Climate*, *24*, 5353–5364. https://doi.org/10.1175/JCLI-D-11-00050.1

Horowitz, L. W. (2006). Past, present, and future concentrations of tropospheric ozone and aerosols: Methodology, ozone evaluation, and sensitivity to aerosol wet removal. *Journal of Geophysical Research*, *111*, DD22211. https://doi.org/10.1029/2005JD006937

Horowitz, L. W., Walters, S., Mauzerall, D. L., Emmons, L. K., Rasch, P. J., Granier, C., et al. (2003). A global simulation of tropospheric ozone and related tracers: Description and evaluation of MOZART, version 2. *Journal of Geophysical Research*, *108*(D24), 4784. https://doi.org/10.1029/2002JD002853

Jia, L., Yang, X., Vecchi, G. A., Gudgel, R. G., Delworth, T. L., Rosati, A., et al. (2015). Improved seasonal prediction of temperature and precipitation over land in a high-resolution GFDL climate model. *Journal of Climate*, *28*, 2044–2062. https://doi.org/10.1175/JCLI-D-14-00112.1

Jickells, T. D., An, Z. S., Andersen, K. K., Baker, A. R., Bergametti, G., Brooks, N., et al. (1996). The NCEP/NCAR 40-year reanalysis project. *Bulletin of the American Meteorological Society*, *77*, 437–471. https://doi.org/10.1175/1520-0477(1996)077<0437:TNYRP>2.0.CO;2

Jickells, T. D., An, Z. S., Andersen, K. K., Baker, A. R., Bergametti, G., Brooks, N., et al. (2005). Global iron connections between desert dust, ocean biogeochemistry, and climate. *Science*, *308*, 67–71. https://doi.org/10.1126/science.1105959

Karyampudi, V. M., & Pierce, H. F. (2002). Synoptic-scale influence of the Saharan air layer on tropical cyclogenesis over the eastern Atlantic. *Monthly Weather Review*, *130*, 3100–3128. https://doi.org/10.1175/1520-0493(2002)130<3100:SSIOTS>2.0.CO;2

Kim, H.-M., Webster, P. J., & Curry, J. A. (2011). Modulation of North Pacific tropical cyclone activity by three phases of ENSO. *Journal of Climate*, *24*, 1839–1849. https://doi.org/10.1175/2010JCLI3939.1

Kim, H.-S., Vecchi, G. A., Knutson, T. R., Anderson, W. G., Delworth, T. L., Rosati, A., et al. (2014). Tropical cyclone simulation and response to CO_2 doubling in the GFDL CM2.5 high-resolution coupled climate model. *Journal of Climate*, *27*, 8034–8054. https://doi.org/10.1175/JCLI-D-13-00475. 1

Kucharski, F., Syed, F. S., Burhan, A., Farah, I., & Gohar, A. (2015). Tropical Atlantic influence on Pacific variability and mean state in the twentieth century in observations and CMIP5. *Climate Dynamics*, *44*(3), 881–896. https://doi.org/10.1007/s00382-014-2228-z

Levin, Z., Ganor, E., & Gladstein, V. (1996). The effects of desert particles coated with sulfate on rain formation in the Eastern Mediterranean. *Journal of Applied Meteorology*, *35*, 1511–1523. https://doi.org/10.1175/1520-0450(1996)035<1511:TEODPC>2.0.CO;2

Lin, N., Smith, J. A., Villarini, G., marchok, T. P., & Baeck, M. L. (2010). Modeling extreme rainfall, winds and surge from Hurricane Isabel (2003). *Weather and Forecasting*, *25*, 1342–1361. https://doi.org/10.1175/2010WAF2222349.1

Liu, J., Mauzerall, D. L., & Horowitz, L. W. (2009). Evaluating inter-continental transport of fine aerosols: (2) Global health impact. *Atmospheric Environment*, *43*, 4339–4347. https://doi.org/10.1016/j.atmosenv.2009.05.032

Mahajan, S., Evans, K. J., Truesdale, J. E., hack, J. J., & Lamarque, J.-F. (2012). Interannual tropospheric aerosol variability in the late twentieth century and its impact on Tropical Atlantic and West African climate by direct and semidirect effects. *Journal of Climate*, *25*, 8031–8055. https://doi.org/10.1175/JCLI-D-12-0029.1

Mahowald, N. M., Kloster, S., Engelstaedter, S., Moore, J. K., Mukhopadhyay, S., McConnell, J. R., et al. (2010). Observed 20th century desert dust variabiility: Impact on climate and biogeochemistry. *Atmospheric Chemistry and Physics*, *10*, 10,875–10,893. https://doi.org/10.5194/acp-10-10875-2010

Miller, R. L., Knippertz, P., Garcia-Pando, C. P., Perwitz, J. P., & Tegen, I. (2014). Impact of dust radiative forcing upon climate. In P. Knippertz & J.-B. W. Stuut (Eds.), *Mineral dust: A key player in the Earth system* (pp. 327–357). Dordrecht, Netherlands: Springer. https://doi.org/10.1007/978-94-017-8978-3_13

Miller, R. L., & Tegen, I. (1998). Climate response to soil dust aerosols. *Journal of Climate*, *11*, 3247–3267. https://doi.org/10.1175/1520-0442(1998)011<3247:CRTSDA>2.0.CO;2

Miller, R. L., Tegen, I., & Perlwitz, J. (2004). Surface radiative forcing by soil dust aerosols and the hydrologic cycle. *Journal of Geophysical Research*, *109*, D04203. https://doi.org/10.1029/2003JD004085

Murakami, H., Vecchi, G. A., Underwood, S., Delworth, T. L., Wittenberg, A. T., Anderson, W. G., et al. (2015). Simulation and prediction of category 4 and 5 hurricanes in the high-resolution GFDL HiFLOR coupled climate model. *Journal of Climate*, *28*, 9058–9079. https://doi.org/10.1175/JCLI-D-15-0216. 1

Patterson, E. M., Gillette, D. A., & Stockton, B. H. (1977). Complex index of refraction between 300 and 700 nm for Saharan aerosols. *Journal of Geophysical Research*, *82*(21), 3153–3160. https://doi.org/10.1029/JC082i021p03153

Prospero, J. M., Ginoux, P., Torres, O., Nicholson, S. E., & Gill, T. E. (2002). Environmental characterization of global sources of atmospheric soil dust identified with the NIMBUS 7 total ozone mapping spectrometer (TOMS) absorbing aerosol product. *Reviews of Geophysics*, *40*(1), 1002. https://doi.org/10.1029/2000RG000095

Prospero, J. M., & Lamb, P. J. (2003). African droughts and dust transport to the Caribbean: Climate change implications. *Science*, *302*, 1024–1027. https://doi.org/10.1126/science.1089915

Reale, O., Lau, K. M., da Silva, A., & Matsui, T. (2014). Impact of assimilated and interactive aerosol on tropical cyclogenesis. *Geophysical Research Letters*, *41*, 3282–3288. https://doi.org/10.1002/2014GL059918

Ridley, D. A., Heald, C. L., & Prospero, J. M. (2014). What controls the recent changes in African mineral dust aerosol across the Atlantic? *Atmospheric Chemistry and Physics*, *14*, 3583–3627. https://doi.org/10.5194/acpd-14-3583-2014

Royer, J.-F., Chauvin, F., Timbal, B., Araspin, P., & Grimal, D. (1998). A GCM study of the impact of greenhouse gas increase on the frequency of ocurrence of tropical cyclones. *Climate Change*, *38*, 307–343. https://doi.org/10.1023/A:1005386312622

Schreck, C. J., Knapp, K. R., & Kossin, J. P. (2014). The impact of best track discrepancies on global tropical cyclone climatologies using IBTrACS. *Monthly Weather Review*, *142*, 3881–3899. https://doi.org/10.1175/MWR-D-1400021.1

Sinyuk, A., Torres, O., & Dubovik, O. (2003). Combined use of satellite and surface observations to infer the imaginary part of refractive index of Saharan dust. *Geophysical Research Letters*, *30*(2), 1081. https://doi.org/10.1029/2002GL016189

Sokolik, I. N., & Toon, O. B. (1999). Incorporation of mineralogical composition into models of the radiative properties of mineral aerosol from UV to IR wavelengths. *Journal of Geophysical Research*, *104*, 9423–9444. https://doi.org/10.1029/1998JD200048

Solmon, F., Elguindi, N., & Mallet, M. (2012). Radiative and climatic effects of dust over West Africa, as simulated by a regional climate model. *Climate Research*, *52*, 97–113. https://doi.org/10.3354/cr01039

Strong, J. D. O., Vecchi, G. A., & Ginoux, P. (2015). The response of the tropical Atlantic and West African climate to Saharan dust in a fully coupled GCM. *Journal of Climate*, *28*, 7071–7092. https://doi.org/10.1175/JCLI-D-14-00797.1

Sun, D., Lau, K. M., & Kafatos, M. (2008). Contrasting the 2007 and 2005 hurricane seasons: Evidence of possible impacts of Saharan dry air and dust on tropical cyclone activity in the Atlantic basin. *Geophysical Research Letters*, *35*, L15405. https://doi.org/10.1029/2008GL034529

Swap, R., Garstand, M., Greco, S., Talbot, R., & Kallberg, P. (1992). Saharan dust in the Amazon Basin. *Tellus Series B*, *44*, 133–149. https://doi.org/10.1034/j.1600-0889.1992.t01-1-00005.x

Tegen, I., & Lacis, A. A. (1996). Modeling of particle size distribution and its influence on the radiative properties of mineral dust aerosol. *Journal of Geophysical Research*, *101*, 19,237–19,244. https://doi.org/10.1029/95JD03610

Tie, X., Madronich, S., Walters, S., Edwards, D. P., Ginoux, P., Mahowald, N., et al. (2005). Assessment of the global impact of aerosols on tropospheric oxidants. *Journal of Geophysical Research*, *110*, LD03204. https://doi.org/10.1029/2004JD005359

Tippett, M. K., Camargo, S. J., & Sobel, A. H. (2011). A Poisson regression index for tropical cyclone genesis and the role of large-scale vorticity in genesis. *Journal of Climate*, *24*, 2335–2357. https://doi.org/10.1175/2010JCLI3811.1

Vecchi, G. A., Delworth, T., Gudgel, R., Kapnick, S., Rosati, A., Wittenberg, A. T., et al. (2014). On the seasonal forecasting of regional tropical cyclone activity. *Journal of Climate*, *27*, 7994–8016. https://doi.org/10.1175/JCLI-D-14-00158.1

Volz, F. E. (1973). Infrared optical constants of ammonium sulfate, Sahara dust, volcanic pumice, and flyash. *Applied Optics*, *12*(3), 564–568. https://doi.org/10.1364/AO.12.000564

Wang, C., Dong, S., Evan, A. T., Foltz, G. R., & Lee, S.-K. (2012). Multidecadal covariability of North Atlantic sea surface temperature, African dust, Sahel rainfall, and Atlantic hurricanes. *Journal of Climate*, *25*, 5404–5415. https://doi.org/10.1175/JCLI-D-11-00413.1

Wilcox, E. M., Lau, K., & Kim, K.-M. (2010). A northward shift of the North Atlantic Ocean Intertropical Convergence Zone in response to summertime Saharan dust outbreaks. *Geophysical Research Letters*, *37*, L04804. https://doi.org/10.1029/2009GL041774

Woodage, M., & Woodward, S. (2014). UK HiGEM: Impacts of desert dust radiative forcing in a high-resoution atmospheric GCM. *Journal of Climate*, *27*, 5907–5928. https://doi.org/10.1175/JCLI-D-13-00556.1

Yoshioka, M., Mahowald, N. M., Conley, A. J., Collins, W. D., Fillmlore, D. W., Zender, C. S., & Coleman, D. B. (2007). Impact of desert dust radiative forcing on Sahel precipitation: Relative importance of dust compared to sea surface temperature variations, vegetation changes, and greenhouse gas warming. *Journal of Climate*, *20*, 1445–1467. https://doi.org/10.1175/JCLI4056.1

Zhang, H., McFarquhar, G. M., Cotton, W., & Deng, Y. (2009). Direct and indirect impacts of Saharan dust acting as cloud condensation nuclei on tropical cyclone eyewall development. *Geophysical Research Letters*, *36*, L06802. https://doi.org/10.1029/2009GL037276

Zhang, H., McFarquhar, G. M., Saleeby, S., & Cotton, W. (2007). Impacts of Saharan dust as CCN on the evolution of an idealized tropical cyclone. *Geophysical Research Letters*, *34*, L14812. https://doi.org/10.1029/2007GL029876

Zhao, M., Held, I. M., Lin, S.-J., & Vecchi, G. A. (2009). Simulations of global hurricane climatology, interannual variability, and response to global warming using a 50-km resolution GCM. *Journal of Climate*, *22*, 6653–6678. https://doi.org/10.1175/2009JCLI3049.1